

# Estimation of the radiation budget during MOSAiC based on ground-based and satellite remote sensing observations

Carola Barrientos-Velasco<sup>1,2</sup>, Christopher J. Cox<sup>3</sup>, Hartwig Deneke<sup>1</sup>, J. Brant Dodson<sup>4</sup>, Anja Hünerbein<sup>1</sup>, Matthew D. Shupe<sup>3,5</sup>, Patrick C. Taylor<sup>6</sup>, and Andreas Macke<sup>1</sup>

<sup>1</sup>Leibniz Institute for Tropospheric Research, Leipzig, Germany

<sup>2</sup>Department of Atmospheric and Oceanic Sciences, McGill University, Montreal, QC, Canada

<sup>3</sup>NOAA, Physical Sciences Laboratory, Boulder, Colorado, USA

<sup>4</sup>Science Systems and Applications, Inc., Hampton, VA 23666, USA

<sup>5</sup>Cooperative Institute for Research in Environmental Sciences, University of Colorado, Boulder, Colorado, USA

<sup>6</sup>NASA Langley Research Center, Hampton, VA, USA

**Correspondence:** Carola Barrientos-Velasco (carola.barrientos-velasco@mcgill.ca)

**Abstract.** An accurate representation of the radiation budget is essential for investigating the radiative effect that clouds have impact of clouds on the climate system, especially in the Arctic, an environment highly sensitive to complex and rapid environmental changes. In this study, we analyse a unique dataset of observations from the central Arctic made during the MOSAiC (Multidisciplinary drifting Observatory for the Study of Arctic Climate) expedition in conjunction with state-of-the-art satellite products from CERES (Clouds and the Earth's Radiant Energy System) to investigate the radiative effect of clouds and radiative closure at the surface and the top of the atmosphere (TOA). We perform a series of radiative transfer simulations using derived cloud macro- and microphysical properties as inputs to the simulations for the entire MOSAiC period, comparing our results to collocated satellite products and ice-floe observations. The radiative closure biases were generally within the instrumental uncertainty, indicating that the simulations are sufficiently accurate to realistically reproduce the radiation budget during MOSAiC. Comparisons of the simulated radiation budget relative to CERES show similar values in the terrestrial flux but relatively large differences in the solar flux, which is attributed to a lower surface albedo and a possible underestimation of atmospheric opacity by CERES. While the simulation results were consistent with the observations, more detailed analyses reveal an overestimation of simulated cloud opacity for cases involving geometrically thick ice clouds. In the annual mean, we found that the presence of clouds leads to a loss of  $5.2 \text{ W m}^{-2}$  of the atmospheric-surface system to space, while the surface gains  $25.25 \text{ W m}^{-2}$ , and the atmosphere is cooled by clouds by  $30.2 \text{ W m}^{-2}$  during the MOSAiC expedition.

## 1 Introduction

In recent decades, the Arctic has undergone one of the most rapid changes in climate and ecosystem dynamics on Earth (Serreze and Barry, 2011). Characterised by its unique climatic conditions, the warming in the Arctic region is considered a robust feature of climate change (Meredith et al., 2019). Among the various factors influencing the Arctic climate, clouds have emerged as critical and important components that play a crucial role in The German (AC)<sup>3</sup> project has been established to investigate the mechanisms responsible for this warming (Wendisch et al., 2023). Clouds are important for regulating regional

and global climate systems (Huang et al., 2017; Tan and Storelvmo, 2019; Zib et al., 2012). Understanding the properties and effects of Arctic clouds is of great importance thus a key goal of (AC)<sup>3</sup> as well as the present paper, as they both respond to and drive climate change in this sensitive polar environment (Morrison et al., 2012; Kay et al., 2016; Taylor et al., 2022, 2023).

Despite the extreme weather and pristine conditions, several efforts have been made over time to improve the quantity and quality of observations of Arctic clouds and their radiative characteristics. A general description of the long-term Arctic stations is presented in Uttal et al. (2016). The stations mentioned in Uttal et al. (2016) have been pioneering lead observation sites to further investigate and explain processes and feedback mechanisms in the Arctic region related to regional processes and transport, the atmosphere, and atmosphere-surface exchanges.

Seasonal airborne Airborne and shipborne research campaigns have been crucial in collecting atmospheric and surface observations in unexplored regions with limited observations, where processes related to this rapidly changing environment remain elusive (see Table 1 in Wendisch et al. (2019)). In addition to these extensive efforts, the Multidisciplinary drifting Observatory for the Study of Arctic Climate (MOSAIC) expedition, conducted from October 2019 to September 2020 (Shupe et al., 2020), aimed to extend the collection of relevant observations related to the Arctic environment. This international collaboration of unprecedented magnitude for an Arctic research cruise provided diverse in-situ and remote sensing observations, allowing investigation of various processes related to Arctic clouds and their interactions with the Arctic system (Shupe and Rex, 2022).

Satellite observations of clouds have particular advantages due to their spatial coverage and long duration of service (Stubenrauch et al., 2013; Christensen et al., 2016; Huang et al., 2017). For instance, Eastman and Warren (2010) compared surface cloud observations with data sets from the Advanced Very High Resolution Radiometer (AVHRR) and Television and Infrared Observation Satellite (TIROS) Operational Vertical Sounder (TOVS). Their comparison highlighted the difficulty in finding agreement between both points of view and the additional challenges encountered during polar night, especially over icy surfaces. Additionally, Hartmann and Ceppi (2014) observed large changes in the Arctic radiation budget at the top of the atmosphere (TOA) based on CERES (Clouds and the Earth's Radiant Energy System) observations, with trends of  $-5 \text{ W m}^{-2}$  and  $3 \text{ W m}^{-2}$  per decade for the shortwave and longwave net fluxes, respectively. The trend analysis focused on the Duncan et al. (2020) analyse the trends in the surface radiation budget of the Arctic boreal zone considering the using CERES Energy Balanced and Filled (EBAF) data products from 2001 to 2017 and reported report a decrease of the reflected solar radiation by  $1.3 \pm 0.6 \text{ W m}^{-2}$  per decade and an increase of the outgoing terrestrial radiation by  $1.1 \pm 0.4 \text{ W m}^{-2}$ , results that suggest a greening effect of Arctic tundra that contribute to a decadal decrease of the surface albedo (Duncan et al., 2020). The study per decade suggesting a greening of the Arctic tundra. These results are subject to the overall monthly uncertainty of  $3 \text{ W m}^{-2}$  for the solar and terrestrial fluxes (Loeb et al., 2018).

The study by Lelli et al. (2023) extensively analysed the regional and seasonal radiative influence effects of clouds on radiation, based on GOME and SCIAMACHY observations over two decades. This study found research revealed that the reduction in Arctic albedo at the top of the atmosphere is compensated by the offset by an increase in atmospheric reflectivity due, attributed to a significant increase in liquid-phase clouds. This increase is dependent on changes in the regional Arctic climate and the underlying surface type. It is important to note that their findings are affected by uncertainties in cloud properties of  $\pm 0.4 \%$ , which have a spatial impact but not a temporal one (see their Appendix E). More recently, Cesana et al. (2024) found

a correlation between Arctic sea ice, cloud phase and radiation based on A-train satellites and CERES observations. This study found that as sea ice cover decreases, the frequency of liquid clouds is more likely to increase leading to a cooling the surface, damping the surface warming during polar day.

Considering satellite and ground-based inter-comparisons, the investigation The investigations by Dong et al. (2016) and Riihelä et al. (2017) compared ground- and satellite-based flux observations in a series of radiative closure studies for the ARM NSA Atmospheric Radiation Measurement (ARM) program's North Slope of Alaska (NSA) site, and the Tara drifting ice camp and observations on the Greenland Ice Sheet, respectively. Both studies considered the CERES Synoptic 1-degree daily flux (SYN1deg) product (Minnis et al., 2021), and found a good agreement based on ground radiative flux observations that were within instrumental uncertainties. The study of Barrientos-Velasco et al. (2022) investigated the effect of clouds on the radiation budget for the early summer PS106 shipborne campaign (Macke and Flores, 2018; Wendisch et al., 2019) and made a comparison between shipborne measurements and collocated satellite products and observations from CERES SYN1deg Ed.4 (hereafter denoted as CERES SYN). Barrientos-Velasco et al. (2022) found that for PS106 the solar radiation dominated the cloud radiative effect by cooling the surface by  $-8.8 \text{ W m}^{-2}$  and the TOA by  $-48.4 \text{ W m}^{-2}$ . This analysis also evaluated cloud macro and microphysical retrievals based on active and passive shipborne remote sensing observations highlighting the frequent underestimation of cloud optical thickness and identifying additional challenges in cloud retrievals during low-level-stratus clouds (Griesche et al., 2023).

More recently, the study by Huang et al. (2022) investigated the sources of uncertainties in the Arctic surface radiation budget derived from CERES, with a particular focus on the representation of surface albedo during the MOSAiC. They found that CERES SYN1deg products underestimated the surface albedo by approximately 0.15 relative to the surface observations and underestimated the atmospheric optical thickness.

To extend the latter analysis and further exploit the capabilities of ground-based and satellite observations, in this paper, we analyse 1D radiative transfer simulations with a focus on the unprecedented yearlong international and interdisciplinary MOSAiC expedition carried out on board the research vessel (RV) *Polarstern* (Shupe and Rex, 2022) that collected unique observations of the ocean (Rabe et al., 2022), sea ice (Nicolaus et al., 2022), and atmosphere (Shupe et al., 2022) properties in the central Arctic. The objective of this paper is to quantify and examine the radiation budget during MOSAiC based on ship-borne and satellite-based remote sensing observations and products, and to evaluate the radiative effect of clouds during MOSAiC at the surface (SFC) and the TOA. Our research questions are as follows:

1. How well can state-of-the-art cloud remote sensing retrievals and radiative transfer calculations represent the Arctic radiation budget and cloud radiative effects?
2. How does the radiation budget vary during the full annual cycle covered by the MOSAiC expedition?
3. What is the radiative effect of clouds on the radiation budget during MOSAiC?

The manuscript is subdivided into the following sections: Section 2 describes the observations and products used in this article. Section 3 details the methodology used for the analysis, followed by Section 4, which presents the results and discus-

sions in several subsections that focus on the analysis at the surface and the TOA. Finally, the article concludes in Section 5, presenting the summary, conclusions, and outlook.

## 2 Observations and datasets

This section provides an overview of the data sources used in this study based on shipborne and ice floe observations, satellite data products, and supplementary datasets.

### 2.1 MOSAiC observations and datasets

Shupe et al. (2022) and Cox et al. (2023e) provide a detailed overview of the atmospheric remote sensing and in situ meteorological observations carried out on board *Polarstern* (PS) and at the MOSAiC Surface Observatory (SO), respectively. In this section, we specifically address the observations used in this study as referenced in Table 1.

#### 2.1.1 Ship-borne instrumentation

On board *Polarstern* there was a suite of active and passive remote sensing instruments used to observe cloud and aerosol properties during MOSAiC. This instrumentation was installed at on *Polarstern*'s bow foredeck at about 10 metres above sea level (see Fig. 3 in Shupe et al. (2022)). As part of the ARM Mobile Facility (Miller et al., 2016), a 35-GHz Ka-band ARM Zenith Radar (KAZR) provided information on radar reflectivity, mean Doppler velocity, and spectrum width (Johnson et al., 2014; Wang et al., 2022). A high spectral resolution lidar and a Micropulse lidar were installed providing information about the backscatter and depolarisation ratio (Morris et al., 1996; Sivaraman et al., 2019). Atmospheric liquid water path (LWP) was derived from the combination of two microwave radiometers, a two-channel sensor (Zhang, 1996) and a **Microwave Radiometer for Arctic Clouds (MiRAC-P)** (Ebell et al., 2022) **Humidity and Temperature Profiler (HATPRO)** (Ebell et al., 2022; Walbröl et al., 2022). In addition, radiosondes were launched every 6 hours from *Polarstern* to provide information about the thermodynamic and kinematic state of the atmosphere (Maturilli et al., 2021).

The **synergistic combination of these instruments and radiosondes combination of instruments and radiosonde observations** is used to **characterise characterize** cloud and aerosol properties during MOSAiC. Section 3.1 summarises the methodology **implemented used** to derive the **cloud** macro and microphysical properties of clouds.

#### 2.1.2 Ice floe observations

During the MOSAiC expedition, several observations of surface and meteorological properties were measured at different locations of the SO. A 10 metre meteorological tower, **a 23-30 metre mast**, and a radiation station were deployed at Met-City. Three mobile Atmospheric Surface Flux Stations (ASFS), named ASFS-30, ASFS-40 and ASFS-50, were deployed in the MOSAiC distributed network, **but were also used closer to *Polarstern* during some periods**. The spatial **coverage distance** of these observations ranged from hundreds of metres to approximately 20 kilometres relative to the location of *Polarstern*, as shown in Fig. 3 of Cox et al. (2023e); **the reasons for these changes was logistical and is explained in the referenced literature**.

For this study we use the Met-City and ASFS observations of skin temperature, and broadband terrestrial (Terr) and solar (Sol) upwelling and downwelling radiative fluxes. While upwelling fluxes may express local variability, the downwelling fluxes are considered regionally representative (Rabe et al., 2024). For clarity, the manuscript uses the terms solar and terrestrial radiation to refer to broadband shortwave and longwave radiation, respectively (see List A1).

The temporal coverage of surface radiation observations varied across the MOSAiC period. Observations at Met-City were made from mid-October 2019 to mid-May 2020 followed by data collection from the end of June to July 2020, after which the ice floe broke apart at the edge of the ice pack. From the end beginning of August to mid-September 2020 Met-City observations were made again from a new ice floe farther north. ASFS-30 had the largest temporal coverage and collected data from mid-October 2019 to mid-September 2020, with a few gaps in November 2019, February 2020, May 2020, and the end of August. ASFS-40's observations were continuous from early October 2019 to the end of March 2020, while ASFS-50's observations were made from early October 2019 to mid-September 2020, but with significant data gaps between mid-January and mid-March 2020, and May May into June 2020, and early August 2020. The narrative is general similar for each station; each variable was quality controlled and some smaller gaps were present for several hours due to quality issues and maintenance (Cox et al., 2023e).

The upwelling and downwelling broadband solar radiative fluxes at Met-City were measured by upward-looking and downward-looking Eppley Precision Spectral Pyranometers (PSP; 0.285 - 3.0  $\mu\text{m}$ ), whereas the terrestrial fluxes were measured with Eppley Precision Infrared Radiometers (PIR; 3.5 - 50  $\mu\text{m}$ ) at 1 Hz sampling rate (see Table 1 in Cox et al. (2023e)). At ASFS stations, downward and upward-looking pyranometers were Hukseflux SR30-D1 and pyrgeometers were IR20-T2 (Cox et al., 2023e). The skin temperature provided at all four sites was derived using information from both upwelling and downwelling terrestrial observations, assuming a surface emissivity of 0.985 (see Eq. 3 in Cox et al. (2023e)). The sensor heights were approximately 2 m above the surface.

## 2.2 Satellite observations and ancillary data

This study uses the CERES SYN1deg Ed. 4 satellite products with hourly resolution (Gupta et al., 2010; Rose et al., 2013; Rutan et al., 2015; Kato et al., 2018; Minnis et al., 2021), referred to here as CERES SYN. The data includes global coverage of solar and terrestrial radiative fluxes at the top of the atmosphere and at the surface with a spatial resolution of 1° latitude by 1° longitude. Fluxes at the top-of-atmosphere are inferred from CERES radiance observations using empirical angular directional models. Fluxes within the atmosphere and at the surface are calculated using the four-stream Langley Fu-Liou radiative transfer model (Fu and Liou, 1992, 1993; Fu et al., 1998; Kratz and Rose, 1999; Kato et al., 1999, 2005) (Fu and Liou, 1992; Kato et al., 2005), adjusting inputs to ensure consistency with the TOA fluxes. The cloud properties used in these calculations were derived from Moderate Resolution Imaging Spectroradiometer (MODIS) radiances (Minnis et al., 2021) Temporal interpolation is achieved at lower latitudes by means of geostationary satellite observations, while relying on the improved temporal sampling of polar-orbiting satellites in polar regions. The CERES SYN product products also use atmospheric reanalysis data from the Global Modeling Assimilation Office Goddard Earth Observing System (GEOS-5) model version 5.4.1 as ancillary input (Rienecker, 2008). Furthermore, surface spectral albedo is based on lookup tables from Jin et al.

(2004) and the broadband albedo is based on Terra surface albedo history maps that are consistent with clear-sky TOA albedo estimates from CERES measurements (Rutan et al., 2015).

The CERES SYN radiative fluxes are given **assuming considering** four different atmospheric **conditions**. **The first is the scenarios**. **An all-sky (AS) conditionatmosphere**, which takes into account both clouds and aerosols**in the atmosphere**. **The second is the . A cloudless sky (CS) conditionatmosphere**, which considers only the presence of aerosols**in the atmosphere**. **The third is the . A pristine (Pr) conditionatmosphere**, where there are no clouds or aerosols **are present**. Finally, **the fourth condition is an all-sky no aerosols (NAER) atmosphere**, where clouds are present, but no aerosols are considered. **The CERES SYN dataset provides radiative fluxes at the surface and at the TOA, which is defined for the calculations as 20 km**.

Besides the radiative flux datasets, various surface, cloud, and aerosol parameters are included in the CERES SYN dataset. Considered in this study are cloud base pressure ( $P_B$ ), cloud top pressure ( $P_T$ ), cloud top temperature, cloud base temperature, cloud fraction (CF), LWP, ice water path (IWP), liquid droplet effective radius  $r_{E,L}$ , and ice crystal effective radius  $r_{E,I}$ . **The CERES SYN product latter products are available for the entire atmospheric column and at four different heights (i.e. surface to 700 mb, 700 to 500 mb, 500 to 300 mb, and higher than 300 mb)**. **The CERES SYN products use the aerosol optical depth (AOD) obtained from the Model of Atmospheric Transport and Chemistry (MATCH; Collins et al. (2001)) data that assimilates retrievals from MODIS (Rutan et al., 2015)**.

### 2.3 Ancillary data

Several ancillary datasets were used as input parameters for the radiative transfer simulations and overall analysis in this article. **Pressure We used pressure** level profiles of temperature, pressure, ozone mass mixing ratio and specific humidity from the European Centre for Medium-Range Weather Forecasts (ECMWF) Re-Analysis (ERA5) (Hersbach et al., 2020) at 1-hour resolution and  $0.25^\circ$  spatial latitudinal and longitudinal resolution. Additionally, dry-air mole **fraction from the fractions of** carbon dioxide, nitrous oxide, methane, **chlorofluorocarbon (CFC) 11, chlorofluorocarbons, specifically CFC-11 and CFC-12**, and Carbon tetrachloride ( $\text{CCl}_4$ ) from the NOAA Global Monitoring Laboratory's annual greenhouse gas index (AGGI; <https://gml.noaa.gov/aggi/aggi.html>) **was used**. **The aforementioned radiosoundings were were used**. **To characterize the atmosphere, we used radiosondes data that was** processed to remove **in the** influence of *Polarstern* and blended with Met-City data to better represent near-surface meteorology, as the radiosondes were launched from the deck at approximately 20 m height (Dahlke et al., 2023).

## 3 Methodology

**This section is divided into two parts. The first part gives an overview of the ShupeTurner cloud retrievals, and the second part addresses the methodology implemented for the radiative transfer simulations.**

### 3.1 ShupeTurner cloud retrievals for MOSAiC

The ShupeTurner cloud retrievals provide time-resolved vertical profiles of the macro- and microphysical properties of clouds based on active and passive remote sensing observations. The retrievals were first introduced in Shupe et al. (2015) (hereafter ST2015) and applied to observations at [Utqiavik, Alaska NSA site](#) (71.323°N, 156.615°W), for the two-year period from March 2004 to February 2006. ST2015 describes the algorithm, including both its assumptions and uncertainties. Moreover, a comparison with the ARM Microbase cloud product (Dunn et al., 2011), as well as a closure analysis of solar and terrestrial downward fluxes have been presented. [The results in ST2015 indicated that ShupeTurner performed better than the ARM Microbase cloud retrievals.](#)

As applied to MOSAiC, the ShupeTurner retrievals utilise cloud radar, depolarisation lidar, microwave radiometer, ceilometer, and radiosonde observations collected on board *Polarstern* as inputs (see Table 1). Reflectivities from the KAZR radar were adjusted above 3 km to statistically match the observations below 3 km due to a known calibration offset between two different radar operational modes. The low-level measurements have been determined to have the best calibration during MOSAiC. Short gaps in [the KAZR data were filled by using](#) a co-located W-band cloud radar, [which were also calibration adjusted to match the KAZR atmospheric profiles of temperature, pressure and humidity were obtained from the radiosondes.](#) [The calibration of this radar was adjusted to align with temporally adjacent KAZR measurements.](#) The LWP data was taken from either of the two microwave radiometers to ensure [maximal maximum](#) coverage.

Several improvements beyond ST2015 were made in the cloud phase classification (Shupe, 2007). A novel set of thresholds were developed from the cloud-free background on the Micropulse lidar depolarisation ratio signal-to-noise and total backscatter measurements using the MOSAiC data. The cloud phase was also corrected to account for lidar attenuation in the presence of liquid-containing cloud layers. For such cases, if the cloud radar observed a cloud top that is within 750 m, then the same cloud type is considered from the attenuation height up to the cloud top. In contrast to the retrievals for [Utqiavik, Alaska, NSA site](#), the default liquid droplet effective radius was changed from 8  $\mu\text{m}$  to 9  $\mu\text{m}$ , which is based on aircraft measurements from the region (Shupe et al., 2005).

[The ShupeTurner products provide information on cloud type phase as well as the content of liquid \(LWC\) and ice water \(IWC\).](#) Effective radius is also calculated for liquid droplets ( $r_{E,L}$ ) and ice crystals ( $r_{E,I}$ ), along with the vertical integral of LWP and IWP.

[ShupeTurner products provides information on cloud type phase as well as the content of liquid \(LWC\) and ice water \(IWC\).](#) The dataset has a 1-minute time resolution and covers a vertical range from 160 m up to 18 km by 596 equidistant height layers, each with a thickness of 30 m.

### 3.2 Single column radiative transfer configuration

The radiative transfer simulations are [obtained from carried out with](#) the TROPOS Cloud and [Aerosol Aerosols](#) Radiative effect Simulator (hereafter TCARS), [which is](#) a Python-based framework [that carries out for](#) 1D radiative transfer simulations [using the interfaces with interfaces to a number](#) of radiative transfer models. Parts of this framework have already been applied and

described in previous studies (Barlakas et al., 2020; Witthuhn et al., 2021; Barrientos-Velasco et al., 2022; Griesche et al., 2023, 2024). TCARS uses various sources of can use various sources for input data such as atmospheric profiles of trace gases, temperature, humidity, properties of clouds, aerosols, cloud properties, and surface parameters. The present study employs the widely used rapid radiative transfer model (RRTM) for GCM applications as solver (RRTMG; Mlawer et al. (1997); Barker et al. (2003); Clough et al. (2005)). The RRTMG model operates with a Python interface Python interface pyRRTMG, version 0.9.1 detailed in Deneke (2024), (Deneke, 2024), is used by TCARS. The overall workflow of the TCARS framework is shown in Figure A1 detailing the input parameters and the output variables derived from the radiative transfer simulations.

The input parameters for the radiative transfer simulation configuration are listed in Table 1. For the atmospheric profiles of temperature, pressure, humidity and ozone, we use hourly pressure level profiles from ERA5, which assimilate information from the Vaisala Radiosonde RS41 that were launched every 6 hours during MOSAiC (Hersbach et al., 2020). This dataset was selected due to its consistent temporal and spatial coverage and well-resolved atmospheric data covering up to 20 km as well as showing good similarities with radiosonde observations (Fig. B1). For trace gases, we used the uniformly distributed values of CO, CO<sub>2</sub>, CH<sub>4</sub>, N<sub>2</sub>O, CCl<sub>4</sub>, CFC-12, HCFC-22 and CFC-11, from the Annual Greenhouse Gas Index (AGGI).

The atmospheric profiles of cloud properties are based on ShupeTurner retrievals. The information added to the model is the LWC, IWC, liquid droplet droplet effective radius ( $r_{E,L}$ ), and ice crystal effective radius ( $r_{E,I}$ ). The RRTMG parameterizations selected for ice and liquid cloud optical properties are based on the radiative transfer model Streamer (Key, 1996) and Hu and Stamnes (1993), respectively. The parameterization of  $r_{E,L}$  in RRTMG only allows values in the range from 2.5 to 60  $\mu\text{m}$ . The parameterization for ice clouds in RRTMG assumes spherical ice crystals shape to be consistent with ShupeTurner assumptions (Sassen, 1987; Atlas et al., 1995; Shupe et al., 2015). In this case, RRTMG allows  $r_{E,I}$  within the range between 5.0 and 131.0  $\mu\text{m}$ .

Several experiments were conducted based on different sources of surface albedo datasets (see Fig. B3, Fig. A1). First, the surface albedo from the CERES SYN product was utilised as an input parameter to calculate the radiative fluxes, denoted as TCARSe1. This dataset is interpolated in both space and time to match the position of *Polarstern* at a 1-minute resolution throughout the MOSAiC cruise. We chose to use this dataset as an input parameter since one of our objectives is to quantify flux differences related to cloud properties rather than surface differences. The comparison of ice-floe measured and surface albedo derived from CERES SYN is discussed in Huang et al. (2022).

The second and third sources of surface albedo come from the observations at ASFS-30 and ASFS-50 stations (see Fig. B3). The radiative flux calculations derived from these two sources are referred to as TCARSe2 and TCARSe3, respectively. This observed surface albedo was derived by calculating the daily mean ratio between the broadband upwelling and downwelling solar flux. We opted for a daily average to exclude small-scale temporal variability observed at these stations. Note that the rest of the input parameters for TCARSe2 and TCARSe3 remain the same as TCARSe1.

The objectives of each experiment were: to verify the consistency of radiative flux calculations between TCARS and CERES SYN without adding variables (i.e., TCARSe1); to validate Shupe-Turner retrievals and quantify the radiation budget and cloud radiative effect (i.e., TCARSe2); and to confirm TCARSe2 results while analysing spatial variability (i.e., TCARSe3).

The surface emissivity is set to a constant value based on the fraction of sea ice in the vicinity of *Polarstern*, which is also obtained from CERES SYN product. When the sea ice fraction reaches or exceeds 50 %, a constant surface emissivity of 0.9999 is used. If the sea ice fraction is below this threshold, a constant of 0.9907 is used instead. These constant values are based on Wilber et al. (1999). It is worth mentioning that this assumption is not the same as the one assumed for deriving the skin temperature from surface measurements (see Eq. 3 in Cox et al. (2023e)). However, we expect that this difference does not exceed by more than  $1 \text{ W m}^{-2}$  the Terr-U at the surface during cloudless conditions (see Table A2 in Barrientos-Velasco et al. (2022)).

Skin temperature is obtained from the derived product by Cox et al. (2023b) at station ASFS-30 due to its extensive temporal coverage. When this data is unavailable, skin temperature from Met-City is utilised (Cox et al., 2023a). In instances when no skin temperature data is available, but the ShupeTurner products are product is available, skin temperature from CERES SYN is used instead for completeness. These latter cases were rare but occurred more frequently in August 2020 (i.e., 2020-08-02 to 2020-08-20).

Several approaches for specifying skin temperature were tested, including using only ERA5 or only CERES SYN. We chose to use derived skin temperature from ice-floe observations at MOSAiC to quantify the flux differences between the CERES SYN product and observations, providing a more realistic calculation of the upwelling terrestrial flux (Terr-U). Another version of the simulations using skin temperature from ERA5 is excluded in this article since this data source led to an overestimation of skin temperature, especially during Polar Nightpolar night, when the largest bias was found during cloudless conditions (see Fig. ??; Herrmannsdörfer et al. (2023)).

All input parameters are linearly interpolated to a predefined standard grid, which consists consisting of 632 atmospheric levelsranging from 40 m up, which range from 40 m to 20 km in altitude, defined as the TOA to be consistent with the definition of TOA from CERES SYN, with. This grid aligns with the CERES SYN TOA height and has a temporal resolution of 1 minute. The first 600 levels of the atmosphere were divided into equidistant layers of 30 m each, and from 18.01 to 20 km, each layer was divided into 63.2 m. In total, 327, 126, and 83 TCARSe1, TCARSe2, and TCARSe3 output daily daily NetCDF files were generated, respectively, with the temporal coverage illustrated in Fig. A2. The generated output files contain vertical Each file profiles of broadband upwelling and downwelling solar and terrestrial fluxes, and heating rates, direct downwelling solar flux for both cloudy and cloudless conditions during the MOSAiC period. (see Fig. A1).

A total of 327, 126, and 83 daily NetCDF files were generated for TCARSe1, TCARSe2, and TCARSe3, respectively. The temporal coverage is illustrated in Fig. A2. For convenience, the simulations have been compiled into monthly files, which are available in Barrientos-Velasco (2024). Each file includes simulated profiles of both cloudy and cloudless broadband upwelling and downwelling solar and terrestrial fluxes, heating rates, and direct downwelling solar flux (see Fig. A1).

This study follows the definition by Rossow and Zhang (1995) and Mace et al. (2006) of the cloud radiative effect (CRE) as the difference in radiation between a cloudy and an atmosphere without clouds cloud free atmosphere at the surface and the TOA. In this article, we discuss two calculation methods: one based on the difference between simulated all-sky conditions minus simulated cloudless conditions, and another term named "hybrid", which subtracts the cloudless simulation from the observed radiative fluxfrom the cloudless simulations. This difference is measured in units of  $\text{W m}^{-2}$ . The Net Total CRE

is calculated by adding the Terr CRE and Sol CRE components, which are calculated using Equation (1). In this equation, “ $x$ ” represents either terrestrial or solar radiation and is calculated at both the surface and the TOA. The atmospheric CRE is defined as the difference between the TOA and the surface. This terminology and methodology are based on previous research by Barrientos-Velasco et al. (2022). A positive value indicates warming, while a negative value indicates cooling due to the presence of clouds.

$$CRE_x = (F_x^\downarrow - F_x^\uparrow)_{All-sky} - (F_x^\downarrow - F_x^\uparrow)_{Cloudless}. \quad (1)$$

## 4 Results and discussions

In this section, we provide a general overview of the atmospheric and surface conditions during MOSAiC. We perform a detailed radiative closure analysis to understand flux biases, followed by an evaluation of the net longwave radiation to infer the atmospheric opacity. The last subsection presents the quantification of the radiation budget using ship-borne and satellite remote sensing observations and products, followed by the investigation of the radiative effect of clouds.

### 4.1 General overview of atmospheric and surface conditions

The RV *Polarstern* drifted with the Arctic sea ice from the Laptev Sea to the Fram Strait, crossing through the central Arctic region from October 2019 to September 2020. For our analysis, we divided the time series into four periods: two during the Polar Night polar night (from October 15 to December 31, 2019, and from January 1 to March 13, 2020) and two during the Polar Day polar day (from March 14 to May 31, 2020, and from June 1 to September 20, 2020) to characterise seasonal differences (Fig. 1). Additionally, we consider the entire MOSAiC period from October 15, 2019, to September 20, 2020.

The second half of October 2019 was characterised by almost featured average near-surface meteorological conditions, with 2-m air temperature decreasing temperatures dropping from about 263 to 255 K (Rinke et al., 2021). This period was characterised by saw a high frequency of single-layer clouds (see Fig. 2a) and a high frequency of occurrence of low-level jets (López-García et al., 2022) that potentially were a source of turbulence into the atmospheric boundary layer contributing to , possibly contributing to turbulence in the atmosphere and a weakly stable atmospheric regime (Jozef et al., 2023). The first storms were observed over Storms began to occur at the MOSAiC location in November. November 16-20 was characterised by , specifically from the 16th to 20th, bringing high winds and moist air from the North Atlantic that caused leads to form and , leading to the formation of leads and causing periodic power outages at the SO that broke the continuity of that disrupted measurements (Nicolaus et al., 2022; Cox et al., 2023e). The lead formation event in mid-November coincides with an intermittent decrease of This lead formation coincided with a decrease in sea ice thickness (Krumpfen et al., 2021). The steady increase of , and integrated water vapour was increased significantly from 2 to 8 kg m<sup>-2</sup> (Heinemann et al., 2023), values that are considered reaching record-breaking in comparison to the levels relative to climatology (Rinke et al., 2021).

During MOSAiC, the The coldest atmospheric conditions were observed from December to mid-March (Herrmannsdörfer et al., 2023). The 2-m air temperature decreased as low as about 231 K , which was the coldest temperature recorded. The

stratospheric temperature also dropped below 200 K 231 K (Fig. ??B2). However, there were two exceptions to this pattern. In early December (December 3-5) and in February (February 18-22), warm air-mass intrusions (WAI) originating from Siberia reached MOSAiC, causing a temporary increase in temperature (Herrmannsdörfer et al., 2023; Rinke et al., 2021). **Contrary to the WAI, a A** marine cold-air outbreak (MCAO) was identified in March with the centre over the Fram Strait region and linked to northerly winds (Rinke et al., 2021; Murray-Watson et al., 2023). From January to March 2020 a record-breaking positive phase of the Arctic Oscillation (AO) index was observed indicating that the low-pressure anomaly in the Arctic was surrounded by a ring of high pressure at mid-latitudes that potentially facilitated the transport of mid-latitude air masses (Lawrence et al., 2020; Rinke et al., 2021; Boyer et al., 2023).

April 2020 was characterised by two WAIs that led to an anomalous increase of near-surface air temperature from 242.4 to 270.0 K from April 14 to April 21 (Shupe et al., 2022). The analysis of Kirbus et al. (2023) suggested that this WAI was associated with a Siberian and Atlantic **pattern air mass** that led to a strong positive effect on the surface energy budget dominated by turbulent heat fluxes over the ocean and strong radiative influence over sea ice. The increase in temperature during this event was associated with the increase in the concentration of water vapour with values that exceeded  $10 \text{ kg m}^{-2}$  (Kirbus et al., 2023). This unprecedented increase in temperature led to several changes in conditions in the atmosphere (Dada et al., 2022; Svensson et al., 2023) and at the surface (Krumpen et al., 2021; Rückert et al., 2023). This period was also used as a first example of the improvement in how nudging a large-scale circulation model to observations improved and accelerated the model evaluation (Pithan et al., 2023).

May was characterised by anomalously warm temperatures that were more prominent during the second half of the month (Rinke et al., 2021). From mid-May to June *Polarstern* left the MOSAiC SO for an exchange of personnel at the fjord of Svalbard (Shupe and Rex, 2022). The months of July and August were considered the warmest **recorded** for the 1979 to 2020 period. The atmospheric conditions during this period were moister than the climatological values **with values of , with the** total column water vapour **reaching** up to  $30 \text{ kg m}^{-2}$  (Rinke et al., 2021). In July 2020, a **large significant** decrease of surface albedo was observed, led by an increase of **pond melt-pond** fraction by 20 % (Webster et al., 2022), especially between July 11 and 13 when melt-pond drainage was observed (Webster et al., 2022; Light et al., 2022).

Finally, in September 2020, the near-surface temperatures started to decrease to temperatures below 273.15 K allowing ice-floe ponds to freeze up (Webster et al., 2022; Light et al., 2022). **Despite the expected decrease of temperature and moisture in the atmosphere for this time of year, two Two** WAI were observed in the middle of September that were associated with an increase in humidity, temperature and heat transport from lower latitudes (Rinke et al., 2021).

## 4.2 Consistency of cloudless simulations

**One of our objectives is to compare surface radiative fluxes from atmospheric radiative transfer simulations based on MOSAiC observations to fluxes from the CERES SYN product. To test the consistency between CERES SYN** Complementing the previous description, Figure 3 illustrates the microphysical cloud properties based on CERES SYN and ShupeTurner. The monthly variation of the LWP and IWP are depicted in box plots and the annual variation of  $r_{E,L}$  and TCARS simulations, we first compared  $r_{E,I}$  are shown at four different heights corresponding to those described in the CERES SYN products (see Section

2.2). For CERES SYN and ShupeTurner, the values of LWP increase during the polar day, which is expected as atmospheric temperature increases. The IWC decreases during summer based on the calculated fluxes for cloudless simulations ShupeTurner dataset, but CERES SYN does not follow the same tendency. It is important to note that the CERES SYN statistics are influenced by periods with optically thick clouds, and there are times when the presence of clouds is either missed or underestimated (see Fig. 2). The  $r_{E,L}$  shows variation with height according to the CERES SYN data, while the ShupeTurner dataset maintains a constant value of  $9 \mu\text{m}$ . Conversely, the  $r_{E,I}$  is greater in the ShupeTurner data compared to the CERES SYN data, showing an overall decrease with height.

## 4.2 Consistency between cloudless fluxes

In this section, we will focus on the TCARSe1 cloudless simulations (see Section 3.2, Fig. A2). The TCARSe1 simulations and CERES SYN product rely on different data sources for atmospheric and surface conditions, such as skin temperature and atmospheric profiles of humidity and temperature. They also use different radiative transfer models. Therefore, prior to conducting the all-sky radiative closure assessment for the MOSAiC period, it is necessary to understand the differences between both fluxes under cloudless conditions. This understanding will be important for the subsequent calculations of the cloud radiative effect.

This analysis focuses on all available TCARSe1 simulations from 2019-10-15 to 2020-09-20 and CERES SYN collocated products products collocated to the location of *Polarstern*. To illustrate the cloudless flux comparison between both datasets, a series of comparative plots are shown in Appendix C. The analysis includes a comparison of downwelling and upwelling terrestrial and solar fluxes at the surface and an upwelling comparison at the TOA. The data set was divided into two periods during polar night and two during polar day as illustrated in Figure 1.

The comparison of cloudless Terr-D at the surface reveals high correlations (over 0.9) between TCARSe1 and CERES SYN shows an agreement with correlations larger than 0.9 and biases no larger than  $9.6 \text{ W m}^{-2}$  (see Fig. ??). The largest discrepancies are from 2019-10-16 to 2019-10-19 and between 2019-11-11 to 2019-11-22 when the , with biases not exceeding  $9.6 \text{ W m}^{-2}$  (not shown). Discrepancies occurred from October 16-19 and November 11-22, where TCARSe1 flux surpasses CERES SYN leading to average flux fluxes exceeded CERES SYN by average differences of  $25.2 \text{ W m}^{-2}$  and  $32.3 \text{ W m}^{-2}$ , respectively. The November period coincided with the WAI described in Section 4.1 (Heinemann et al., 2023). While during this period the cloud occurrence was high, the few cloudless periods identified (i. e., 2019-11-13 6:30Z-22:00Z) indicate a discrepancies coincided with high cloud occurrence during the WAI period. However, a cloudless period on November 13 showed good agreement between the TCARSe1 simulations and observations at the ASFS-40 station with a observations, with mean (maximum) flux difference differences of  $1.8 \text{ W m}^{-2}$  ( $5.3 \text{ W m}^{-2}$ ).

During the spring, in contrast to Polar night months, CERES SYN product show larger Terr-D values than TCARSe1 results (see Fig. ??c). The mean flux difference between both datasets for the period 2020-03-14 to 2020-05-31 is  $3.5 \text{ W m}^{-2}$  and shows the best correlation of 0.98. From June 9, 2020, until the end of MOSAiC, the TCARSe1 cloudless Terr-D fluxes are larger than CERES SYN values as during the 2019-10-15 to 2019-12-31 period (Fig. ??b), but with a smaller magnitude.

The last period with the largest Terr-D flux discrepancies was observed between 2020-08-01 and 2020-08-21, with a mean flux difference of  $13.2 \text{ W m}^{-2}$ . Unfortunately, during this period, no observations at MOSAiC SO were collected; thus, no additional comparison with ice-floe observations could be made to determine which dataset was closer to the observations under cloudless conditions.

The comparison of cloudless Terr-U flux at the surface indicated a consistent agreement between both datasets with biases below  $5.9 \text{ W m}^{-2}$  and correlations larger than  $0.87$  (see Fig. ??). The comparison of skin temperature . However, the skin temperature comparison in Fig. B2 shows a relatively good agreement between CERES SYN and the MOSAiC SO observations for all months except reveals a discrepancy in September 2020, where CERES SYN values are notably lower than the lower than MOSAiC SO observations. The largest difference occurs between 2020-09-14 to 2020-09-20 when the mean and maximum flux difference is  $21.6$  and  $27.5 \text{ W m}^{-2}$  was observed from September 14-20, respectively. This period coincides 2020, with a mean flux difference of  $21.6 \text{ W m}^{-2}$  and a maximum  $27.5 \text{ W m}^{-2}$ , coinciding with two storms with WAI events that brought moisture leading to that caused rain on snow, events described earlier and reported in as noted in prior studies Rinke et al. (2021) and Shupe et al. (2022).

It is noteworthy that the Kernell Density Estimate (KDE) distribution of the cloudless Terr-U flux difference for the period 2019-10-15 to 2019-12-31 shows a bi-modal distribution (see Fig. ??a). Two sub-periods explain the distribution around  $18 \text{ W m}^{-2}$ . The periods between 2019-10-28 to 2019-11-09, and from 2020-12-15 to 2019-12-25 show a mean cloudless Terr-U flux difference of  $11.0 \text{ W m}^{-2}$  and  $10.9 \text{ W m}^{-2}$ , respectively, with the highest differences up to  $35.7 \text{ W m}^{-2}$  as observed for December 21 and 22. Both periods coincide with anomalously cold periods that are lower than the median over 1979-2019 (see Fig. 1 in Rinke et al. (2021)).

The cloudless comparison of Sol-D is illustrated shown in Fig. C1a, b, e, and f. While the correlation coefficient for the comparison is near  $1.0$ , and the distributions reveal an unimodal distribution centred pattern centered near zero for both cloudless and pristine conditions (depicted in green). The mean flux differences for the period between from 2020-03-14 and to 2020-05-31 are  $2.9 \text{ W m}^{-2}$  for cloudless conditions and  $-3.1 \text{ W m}^{-2}$  for pristine conditions.

For the period between From 2020-06-01 and to 2020-09-20, the comparison indicates consistent good agreement between TCARSe1 simulations and CERES SYN pristine products show good agreement. The comparison between CERES SYN cloudless and CERES pristine products suggests that the presence of aerosols reduces Sol-D by about  $6.0 \text{ W m}^{-2}$  during the first Polar polar day period and by  $15.3 \text{ W m}^{-2}$  during the second Polar polar day period.

As all versions of TCARS simulations do not account for the presence of aerosols in the atmosphere, given that the main focus was on the influence of clouds on the radiation budget, these differences due to the presence of aerosols are nonetheless considered in the analysis presented in the following sections.

The mean Sol-U flux difference between TCARSe1 simulated fluxes and the CERES SYN product at the SFC surface is  $2.4 \text{ W m}^{-2}$  for the first Polar polar day period (Fig. C1c) and  $7.2 \text{ W m}^{-2}$  for the second Polar polar day period (Fig. C1d). The comparison between TCARSe1 and CERES SYN pristine products shows biases of  $-2.6 \text{ W m}^{-2}$  and  $-2.0 \text{ W m}^{-2}$  for the respective Polar polar day periods. Differences arise since the presence of aerosols reduces the amount of solar radiation

reaching the surface, thereby decreasing its availability to be reflected. Consequently, the similarity in KDE kernel density estimate (KDE) distributions of Sol-D and Sol-U fluxes reflects the dependence of both components on the radiative transfer calculations.

At the TOA, the cloudless Terr-U and Sol-U fluxes exhibit good agreement between TCARSe1 simulations and CERES SYN product. All correlation coefficients are higher than 0.89, and the distributions are centred around zero. The mean flux differences are below  $\pm 4.5 \text{ W m}^{-2}$  within the instrumental uncertainty and consistent between both datasets (see Fig. ?? and Fig. ??not shown).

In general, the cloudless comparison between TCARSe1 simulations and CERES SYN product suggests a reliable comparison. Nevertheless, it is important to consider the periods during which the disagreement is more significant due to an underestimation of temperature and humidity from CERES SYN leading to an underestimation of the Terr-D flux and the omitted direct influence of aerosols under cloudless conditions reducing the Sol-D flux for TCARS simulations.

### 4.3 Radiative closure assessment

The three versions of TCARS simulations and TCARS sets of simulations (i.e., TCARSe1, TCARSe2, and TCARSe3) and CERES SYN product are evaluated within the context of a radiative closure analysis study that is defined as acceptable if the biases are within the assessed uncertainty of the measurements. To be consistent with previous studies (i.e., Dong et al. (2016); Ebell et al. (2020); Barrientos-Velasco et al. (2022)) we consider acceptable biases no larger than  $\pm 10.0 \text{ W m}^{-2}$  for the Terr-D and  $\pm 20.0 \text{ W m}^{-2}$  for the Sol-D as these values are considered to be the maximum uncertainty in polar regions (Lanconelli et al., 2011). The global annual mean net surface flux uncertainty for CERES SYN product are within  $\pm 12.0 \text{ W m}^{-2}$ , however, larger uncertainties are expected in the polar regions, especially on the upward solar flux (Kato et al., 2012).

The following radiative transfer Barrientos-Velasco et al. (2022) examined how uncertainties in various input parameters, such as atmospheric temperature, water vapour, skin temperature, ozone, and surface albedo, propagate through radiative transfer simulations under clear-sky conditions. The findings indicated that the propagated uncertainty in the radiative fluxes was  $\pm 2.6 \text{ W m}^{-2}$  for the Terr-D and  $\pm 3.7 \text{ W m}^{-2}$  for the Sol-D. Potential uncertainties in the cloud product arise from input measurements, the categorical classification of cloud types, and the retrievals applied, and these interact in complex ways with the variable environmental uncertainties associated with spatial variability and scale mis-matches for different observations and parameters. While it is nearly impossible to disentangle or quantify the individual impacts of these uncertainties, the radiative closure employed here is one means for assessing the overall uncertainty of all components collectively.

The following radiative closure assessment focuses on comparing the simulated terrestrial and solar fluxes with the observed fluxes at the surface and TOA. At the surface, the radiative closure is considered only for downwelling fluxes, while at the TOA, it is considered for upwelling fluxes. The counterparts are not evaluated as they are less dependent on clouds and the simulations use them as inputs, such as skin temperature (e.g., TCARSe1, TCARSe2, TCARSe3) and surface albedo (e.g., TCARSe2, TCARSe3). Moreover, we aim to be consistent with the methodology presented in ST2015.

Additionally, we categorise the comparison by atmospheric conditions into four main categories: All-sky, Cloudy, Cloudless, and Broken Cloud conditions, as classified by ShupeTurner. Broken Cloud conditions were derived from the cloudless

screening and were identified in instances where the standard deviation among downwelling flux observations from stations exceeded  $10.0 \text{ W m}^{-2}$  during periods when more than one downwelling pyranometer or pyrgeometer was available. Including the category of Broken Cloud conditions in the analysis aims to remove any cloud contamination in the cloudless analysis. Achieving a good representation of cloudless conditions is the first step in validating the radiative transfer simulations and separating cases that are outside the scientific objectives of the current study. Our analysis does not further investigate the similarities or discrepancies of cloud phase between ShupeTurner retrievals and CERES SYN product.

The comparison includes all available high-quality ice-floe observations from ASFS stations and at Met-City, while excluding periods with rain. Rainy conditions introduce interference, either by disrupting the microwave radiometer measurements (Cadeddu et al., 2017) or obstructing the view of upward-looking pyranometers and pyrgeometers.

This section is divided into two parts. The first subsection presents a comparison between simulated and observed downwelling terrestrial and solar fluxes at the surface, and the second section compares the upwelling terrestrial and solar fluxes at the TOA.

For clarity, the analysis with TCARS simulations will refer to experiment TCARSe2 for the solar and terrestrial fluxes. Note that the analysis of the terrestrial flux is extended to the data availability of TCARSe1 (Fig. A2), as the parameter that was altered in the input (i.e., surface albedo) does not influence the calculations of terrestrial fluxes.

#### 4.3.1 Analysis at the surface

The hourly comparison between Terr-D simulated fluxes and observations at ASFS-30 shows very good agreement for TCARSe1 TCARSe2 results, with median hourly differences below  $\pm 5 \text{ W m}^{-2}$ , for all-sky, cloudy, and cloudless atmospheric conditions (Fig. 4a, 4b, 4c, Table 2). The comparison with CERES SYN also indicates very good agreement for these conditions. However, larger differences are found for the defined cloudless atmosphere, with a median difference of  $6.5 \text{ W m}^{-2}$  (Table 2). A deeper analysis during this atmospheric condition using CERES SYN cloudless products instead of all-sky products suggest that while cloudless conditions are identified at *Polarstern*, other clouds were present within the spatial resolution of CERES SYN, reducing the biases from  $13.2 \text{ W m}^{-2}$  to  $-9.9 \text{ W m}^{-2}$  (see values in parenthesis in Table 2). For both datasets, TCARSe1 TCARSe2 and CERES SYN, the simulated Terr-D flux for cloudless conditions shows negative biases that are compensated by the presence of clouds. Due to the limitations of the 1D experimental radiative transfer setup from TCARS and CERES SYN, larger biases can be expected under broken cloud conditions, which occurred about 0.6 % of the time (Fig. 4d, 4h, 4l, 4p).

The overall hourly TCARSe1 TCARSe2 Terr-D flux comparison among all stations indicated a good agreement, suggesting that, in general, the Terr-D flux is similar despite the distances separating each station (Fig. D1a). This finding aligns with Rabe et al. (2024), which reported that in transient conditions, the temporal variability of the Terr-D was larger than the spatial variability. The spatial comparison of the collocated CERES SYN product with each station suggests that the mean flux difference is relatively dependent on the location of the observations. According to CERES SYN, the atmospheric conditions might have varied to some extent relative to the location of *Polarstern* (Fig. D2a).

The KDE distribution comparing of the Sol-D flux difference between simulations and observations is illustrated in the second and forth column in Fig. ?? 4 for TCARSe2 and CERES SYN, respectively, and the summary of the biases including all the simulations is shown in Table 3. The lowest biases found are for TCARSe2 with mean and median flux differences below  $\pm 4.1 \text{ W m}^{-2}$  for all-sky and cloudy conditions. The largest biases are found for cloudless conditions for all the simulations, but within the uncertainty threshold of  $\pm 20 \text{ W m}^{-2}$ . In general, the radiative closure can be confirmed for TCARS simulations and CERES SYN.

The Sol-D flux comparison between TCARSe1 and TCARSe2 directly shows the effect that surface albedo has on radiative transfer calculations. Both TCARSe1 and TCARSe2 use the same cloud properties, but the change in surface albedo causes a mean flux difference of about  $10 \text{ W m}^{-2}$  in the Sol-D flux (Table 3). This suggests that a lower surface albedo (i.e., CERES SYN) absorbs more solar radiation at the surface, reducing the reflected solar flux from the surface to the cloud, and thus further decreasing the reflection from the cloud back to the surface. Note that the viewing differences between ground-based and satellite sensors are another factor leading to the flux differences as the ground-based observations cover an area of a few meters. In contrast, the satellite perspective has a viewing area with multiple ice floes and an open ocean. Since the ground measurements are used for the comparisons here, it is not surprising that the TCARSe2 and TCARSe3 datasets would show closer agreement.

In the study of Huang et al. (2022), several perturbation experiments were conducted varying the surface albedo and the cloud fraction. This study found that by increasing the surface albedo and the cloud fraction, the biases in the solar and terrestrial fluxes reduced, stating suggesting that the surface albedo and atmospheric opacity within the CERES SYN product are underestimated. Our results corroborate their findings, but what we find counter-intuitive is that in general the values of LWP and IWP are larger for CERES SYN than for ShupeTurner (Fig. 3). The latter might suggest also be related to the size of cloud liquid droplets. The size of  $r_{E,L}$  is comparatively larger for CERES SYN than ShupeTurner, resulting in a smaller optical depth as less sunlight is reflected. It should also be considered that the cloud parameterizations or set up used when calculating the radiative fluxes vary in a large magnitude significantly between the radiative transfer solver RRTMG and the four-stream Langley Fu-Liou radiative transfer model. While it is outside the scope of this study to investigate model differences, it is reported that the differences between both models are within the uncertainties set by this study of  $\pm 10.0 \text{ W m}^{-2}$  for the Terr-D and  $\pm 20.0 \text{ W m}^{-2}$  for the Sol-D (Gu, 2019).

The analysis of the Sol-D flux utilises observations from ASFS-30 and ASFS-50 (Fig. D1b, Fig. D2b). No observations were available from ASFS-40 during Polar Daypolar day, and measurements from Met-City are excluded due to a systematic error that caused lower Sol-D values for optically thin atmospheres (e.g., cloudless skies or thin ice clouds). The mean Sol-D flux difference between Met-City and ASFS-50 observations varied by approximately  $18 \text{ W m}^{-2}$  under these conditions. The underestimation of Sol-D observed at Met-City during these conditions may be attributable to the instrumental characteristics limitations of the pyranometer at Met-City (i.e., Eppley PSP), which is sensitive to incident viewing angles. More details and implications of this sensitivity for surface-based radiometric reference data sets over the global oceans is discussed in Riihimaki et al. (2024).

The ShupeTurner cloud retrievals were evaluated previously in ST2015 considering two-year atmospheric observations at [Utqiavik, Alaska NSA site](#). The radiative closure assessment in ST2015 focused on the downwelling fluxes at the surface and upwelling fluxes at the TOA. The results discussed here are similar to the results reported in ST2015. The largest median flux difference is for cloudless Sol-D flux with median flux values of  $-15.6 \text{ W m}^{-2}$  whereas in this study the median flux difference is  $3.3 \text{ W m}^{-2}$  (Table 3). The Sol-D flux difference in ST2015 might be due to broken cloud conditions that **possibly were not excluded from had an unquantified impact on** their analysis. Note that the results presented in ST2015 were 10-min averages, whereas here the results are hourly averages.

The analysis of ST2015 further investigated the radiative closure assessment by sub-classifying the cloud phase of single-layer clouds into liquid, ice, and mixed-phase. Doing a similar analysis, [TCARSe1](#) [TCARSe2](#) results indicate a very good agreement for Terr-D flux at the surface for the three thermodynamic conditions (i.e., liquid, ice, and mixed-phase clouds) with hourly median flux differences below  $\pm 4.1 \text{ W m}^{-2}$  (Table A2).

The results for the Sol-D flux comparison considering the three versions of TCARS simulations are shown in Table A3. At the SFC, the best agreements are found for TCARSe2 and TCARSe3, with median flux differences below  $\pm 6.6 \text{ W m}^{-2}$ . When looking at the mean biases, liquid clouds show the best agreement. For ice clouds, there is a positive bias for TCARS of about  $20 \text{ W m}^{-2}$ , suggesting an **overestimation underestimation** in cloud opacity, and in mixed-phase clouds, there is a negative bias of  $8.4 \text{ W m}^{-2}$ . The effect of different surface albedo between TCARSe1 and TCARSe2 in single-layer liquid and mixed-phase clouds leads to a mean flux difference of about  $12.4 \text{ W m}^{-2}$ , suggesting that with a lower surface albedo, less solar radiation is available for multiple reflections between cloud and surface. The same effect is observed for ice clouds, but to a lesser extent ( $4.1 \text{ W m}^{-2}$ ), as they **absorb scatter** Sol-D **less more** effectively.

It is important to note that these results are subject to sample availability and hourly averaging. Increasing the time resolution of the analysis could highlight the influence of advection on observations, thereby enhancing the spatiotemporal variability of the radiative fluxes (Barrientos Velasco et al., 2018; Rabe et al., 2024). Additional analysis on how surface albedo affects the derivation of atmospheric fluxes is recommended for future studies. Improving or refining this parameter is beyond the scope of the current analysis.

### 4.3.2 Analysis at the top of the atmosphere

The comparison of the upwelling [TCARS radiative fluxes and CERES SYN product radiative fluxes](#) at the TOA are illustrated in Fig. 5, Fig. D3 and reported in Tables 4 and 5. The comparison shows the difference between TCARS simulations and the collocated CERES SYN product at the locations of all the stations at MOSAiC SO. Besides evaluating the TCARS simulations at the TOA, we aim to analyse how the spatial coverage influenced the flux differences.

While the mean Terr-U flux differences are similar across all stations, ranging from  $-4.4$  to  $-0.4 \text{ W m}^{-2}$ , the KDE distribution indicates the best agreement **at Met-City. For ASFS-30 above the Met City location. At the AFSF-30 and ASFS-50 , higher distributions are observed for positive values , whereas sites, a higher occurrence of positive values is observed, whereas the ASFS-40 shows a higher occurrence site shows a greater frequency** of negative values (see the first column in Fig. 5). Despite these differences in distribution, the values suggest consistency among [TCARSe1](#) [TCARSe2](#) simulations, indicating a limited

influence of spatial variability (Fig. D3a). Analysis of single-layer liquid, ice, and mixed-phase clouds shows biases lower than  $7.5 \text{ W m}^{-2}$ , confirming the consistency of Terr-U flux in the TCARS results at the TOA (Table A2).

The comparison of the Sol-U flux comprises all the versions of TCARS simulations. Given that the surface albedo observed at MOSAiC SO is higher than CERES SYN (see Fig. B3, (Huang et al., 2022)Huang et al. (2022)), larger Sol-U fluxes are calculated at the TOA for TCARSe2 and TCARSe3 (Table 5). The median Sol-U flux difference is lower in magnitude than the results reported in ST2015 with values ranging between  $17.4$  and  $21 \text{ W m}^{-2}$  for all-sky and cloudy conditions and monomodal distributions around  $0.0 \text{ W m}^{-2}$  (see Fig. 5 second column).

The change in surface albedo affects the calculated Sol-U fluxes by  $15.4 \text{ W m}^{-2}$  during all-sky conditions and up to  $25.0 \text{ W m}^{-2}$  during cloudless conditions. The latter highlights the masking effect that clouds have on TOA reflectance as discussed in Sledd and L'Ecuyer (2019). The results in ST2015 are relatively similar to the ones calculated here for the Terr-U, but the comparison of Sol-U in ST2015 shows larger median flux differences ranging from  $-41.3$  to  $-14.4 \text{ W m}^{-2}$ . It is worth noting that the median flux difference for cloudless conditions in ST2015 is  $-43.1 \text{ W m}^{-2}$ , a considerably larger value that could have been caused by differences in spatial inhomogeneities of surface properties within the satellite spatial resolution in contrast to the single column radiative transfer calculation in ST2015.

The overall comparison of TCARS terrestrial and solar upwelling flux comparison indicates a reasonably fluxes shows consistent agreement with CERES SYN product at the TOA supporting the use the CERES SYN observations at TOA, supporting the reliability of TCARS results to be reliable to calculate as estimates of the radiation budget and extend the analysis of cloud radiative effects during at MOSAiC. Moreover, the differences observed in radiative closure highlight the important role that surface albedo, emphasise the significant role of surface albedo and its spatial scaling, play in when comparing different products.

#### 4.4 Evaluation of net terrestrial radiative flux Radiation budget

In this section, we consider The radiation budget is calculated for the MOSAiC period at the surface and at the TOA, utilising TCARS, CERES SYN datasets, and MOSAiC observations. This section provides both monthly and full-year statistics.

Similarly as the previews section, the analysis of the net terrestrial radiative flux to describe the atmospheric opacity for a non-scattering atmosphere in the terrestrial spectral range. Atmospheric opacity refers to the absorption of solar and terrestrial radiation. A transparent atmosphere is one where no significant solar or terrestrial radiation is absorbed within it. Conversely, an opaque atmosphere absorbs a considerable amount of radiation, while a semi-transparent atmosphere absorbs radiation to a lesser extent than in opaque conditions (Guzman et al., 2017).

We analyse atmospheric opacity by examining variations in the net terrestrial flux (Terr-N; defined as Terr-D minus Terr-U) terrestrial flux considers the TCARSe2 and it is extended to the data availability of TCARSe1. The analysis of solar flux also uses the TCARSe2 simulations, as this variable is related to atmospheric opacity in the terrestrial spectral range. Analysing the distribution of dataset is based on observed daily mean surface albedo from ASFS-30 that has better temporal coverage than TCARSe3 (see Section 3.2, Fig. A2). The calculation of total fluxes (i.e., Terr-N aids in the interpretation and representation of atmospheric conditions in the TCARS and CERES SYN simulations. Additionally, this parameter spans the entire MOSAiC

period, enabling a comprehensive understanding of the monthly atmospheric state plus Sol-N) is based on the aforementioned datasets. The statistical analysis of observed terrestrial fluxes is primarily based on observations from ASFS-30, except for October 2019, when data from Met-City was used due to data availability.

The Note that the analysis of the Terr-N is based on TCARSe1 due to the good temporal coverage. Note that the analysis using TCARSe2 and TCARSe3 simulations was not made, as the analysis would lead the similar results since the only difference among the three sets of experiments is the surface albedo, and this parameter does not influence the Terr flux. **Figure 7**

#### 4.4.1 Analysis at the surface

The Terr-N flux showed large variability with values ranging from around  $-100 \text{ W m}^{-2}$  to positive values around  $25 \text{ W m}^{-2}$  with lower variability during July and August when the Terr-D and Terr-U at the surface are relatively similar because of generally great cloud fraction (Fig. 2, Fig. 6a, Fig. 7k and 7i).

The solar flux at the surface is shown in Figures 6c and 6d. The box plots for TCARSe2 and ASFS-30 exhibit relatively similar patterns across all months. In contrast, the CERES SYN data shows a clear overestimation of the Sol-N flux, primarily due to lower surface albedo values considered in CERES SYN. With an underestimation of surface albedo by  $-21.01 \%$  (Huang et al., 2022), the even higher solar flux suggests an underestimation of atmospheric opacity, as more radiation is absorbed by the surface based on CERES SYN product. The Sol-N values for TCARSe2, CERES SYN, and ASFS-30 are  $23.6$ ,  $34.1$ , and  $22.1 \text{ W m}^{-2}$ , respectively, indicating that TCARSe2 provides a better representation of the observed Sol-N flux than the CERES SYN products for the MOSAiC period (Table 6).

The Total flux at the surface, shows a consistent dominance of the Terr flux for most of the year through March 2020 (Fig. 6e). April is the transition month where the values start to become positive. From May to August 2020 the Net fluxes at the surface are dominated by the Sol fluxes. The first 20 days of September 2020, are also part of a transition mode where the Net fluxes are near  $0 \text{ W m}^{-2}$ . The Total flux at the surface for the MOSAiC period based on TCARS, CERES SYN, and observations is  $1.7$ ,  $15.6$ , and  $3.9 \text{ W m}^{-2}$ , respectively. The over-estimation of the Total flux from CERES SYN is led by the Sol-N by  $27.4 \text{ W m}^{-2}$ , whereas the underestimation in the Terr-N accounts for  $3.0 \text{ W m}^{-2}$ . Using the derived surface albedo from CERES SYN and ShupeTurner retrievals (i.e., TCARSe1) suggests an overall overestimation of the total net flux by  $13.9 \text{ W m}^{-2}$  (Table 6).

Complementary to the box plots shown in panel a and b in Figure 6, we include the KDE distribution for the entire MOSAiC period and for each month (Fig. 7). This plot is included to deepen the understanding of the radiation budget and further investigate the variations of the Terr-N flux during MOSAiC.

Figure 7 shows the Terr-N monthly distribution for TCARSe1. The overall comparison for the entire MOSAiC period is shown in Fig. 7a. The remaining panels provide the distribution for each month. Each distribution is subdivided into two zones. Values greater than  $-25 \text{ W m}^{-2}$  represent an optically thick atmosphere, and values less than  $-25 \text{ W m}^{-2}$  are defined as a semi-transparent atmosphere. **Other thresholds were used in other studies, where a semi-transparent atmosphere is defined from  $-25$  to  $-15 \text{ W m}^{-2}$ , cloudy atmosphere is defined for values greater than  $-15 \text{ W m}^{-2}$  and clear-sky for Terr-N fluxes**

lower than  $-25 \text{ W m}^{-2}$  (e.g., Solomon et al. (2023)). However, here we opted for a threshold that could also be implemented during Polar day as the values of Terr-D and Terr-U are higher.

Each panel in Fig. 7 shows the KDE distribution observed at ASFS-30 (gray), calculated from TCARSe1 (red), and CERES SYN (blue). Additionally, for October and November 2019, the distribution from ASFS-40 (green) is included and for March and April 2020 the observations at Met-City are added (orange). The observations at these stations were added as the observations had more hourly data samples compared to observations at ASFS-30. The comparison of TCARSe1 and CERES SYN product was limited to the data availability of the observations, meaning that if there were any data gaps, the exact hourly sample was removed from TCARSe1 and CERES SYN datasets for a fair comparison. For October and November 2019, the data limitation was based on was limited to the data coverage of ASFS-40 observations and for March and April, the datasets were limited to the data availability at Met-City. The rest of the months were limited to the observations at ASFS-30.

Based on the Terr-N comparison for the entire MOSAiC period, the atmosphere was characterised by a clear bimodal distribution in all seasons, indicating distinct occurrences of optically opaque and optically thin atmospheres. However, for the months of May through September there is a particularly frequent occurrence of optically thick atmospheres, consistent with the frequent occurrence of clouds with high LWP in these months (Fig. 3a). In October 2019, the last 15 days of the month were analysed, and in September 2020, the first 20 days were evaluated, showing relatively similar distributions of Terr-N flux and indicating a higher occurrence of opaque atmospheres.

The TCARSe1 Terr-N distribution generally captures the bimodal distribution observed for most months, although discrepancies arise during certain Polar Night months (e.g., November and December 2019, and January, February, and March 2020), polar night months, where it tends to overestimate the occurrence of the highest opacity cases and underestimate the occurrence of low opacity cases compared to observations.

The CERES SYN Terr-N distributions exhibit considerable discrepancies with both the observed data and TCARSe1 simulations, particularly in the shapes of the KDE distributions, which generally indicate optically thinner atmospheres, as discussed in Section 4.3.1 and previously noted in Huang et al. (2022). Another explanation might be related to the spatial resolution that could smooth out the clear differences between an opaque and semi-transparent atmosphere. The more negative Terr-N values are especially pronounced during Polar Night polar night. In contrast, during Polar Day polar day, the distributions show a better correspondence align more closely with observations. This finding aligns is consistent with Fig. 2, which highlights shows that the months with the largest discrepancies correspond to periods where greatest discrepancies occur when the frequency of CERES SYN cloud fraction is lower than the ShupeTurner Shupe-Turner retrievals.

In February 2020, the CERES SYN Terr-N KDE distribution indicated indicates a more frequent occurrence of semi-transparent atmospheres, leading to . This resulted in an overestimation of cloudless conditions and an underestimation of atmospheric opacity. A detailed analysis of several cases in this month and during September indicated a more frequent underestimation when the cloud base was misidentified during snow precipitation events identified by ShupeTurner (not shown).

September 2020 poses a particularly challenging comparison, as the Terr-N discrepancy stems not only from an underestimation of cloud opacity but also from a significant underestimation of skin temperature, leading to an underestimation of Terr-U flux values in CERES SYN product (see Fig. B2). A comparison using observed Terr-U fluxes at ASFS-30 instead

of Terr-U fluxes from CERES SYN indicates a higher distribution toward a more semi-transparent atmosphere (not shown), making September 2020 the period with the most pronounced underestimation of cloud opacity by CERES SYN. It is worth clarifying that from September 4 to 19, ASFS-30 was positioned over a re-freezing melt pond melt-pond (Cox et al., 2023e), which may also explain these differences.

#### 4.5 Radiation budget and cloud radiative effect (CRE) during MOSAiC Analysis at the TOA

The radiation budget and the CRE are calculated for the MOSAiC period at the surface and at the TOA, utilising TCARS, CERES SYN datasets, and MOSAiC observations. This section provides both monthly and full-year statistics.

The following box plot time series presented in this section examines the TCARSe1 dataset for terrestrial flux, as these simulations cover the entire MOSAiC period. In contrast, the analysis of solar flux illustrated in the box plots uses the TCARSe2 simulations, as this dataset is based on observed daily mean surface albedo from ASFS-30 and they have a longer temporal coverage than TCARSe3 (see Section 3.2, Fig. A2). The calculation of total fluxes (i.e., Terr-N plus Sol-N) is based on the aforementioned datasets. The statistical analysis of observed terrestrial fluxes is primarily based on observations from ASFS-30, except for October 2019, when data from Met-City was used due to data availability. For completeness, we included the calculations of the radiation budget and the CRE based on TCARSe1, and TCARSe3 simulations and reduced the CERES SYN values to the data availability of TCARSe2 simulations for comparison purposes (see Table 6).

Figure 6 shows the terrestrial net (Terr-N, panel a), solar net (Sol-N, panel c), and Net fluxes (panel e) at the surface in monthly box plots. The results for each month are shown for TCARS (in red), CERES SYN (blue) and observations (black). Each month considers the same data points to illustrate a fair comparison among the datasets. The result for the entire MOSAiC period is illustrated in panels b, d and f for the Terr-N, Sol-N, and Total surface flux, respectively.

The Terr-N flux showed large variability with values ranging from around  $-100 \text{ W m}^{-2}$  to positive values around  $25 \text{ W m}^{-2}$  with lower variability during July and August when the Terr-D and Terr-U at the SFC are relatively similar because of generally high cloud fraction (Fig. 2, Fig. 7k and 7i, Fig. 6a).

The variation of the upwelling and downwelling Terr fluxes at the SFC is comparable to other sites in the Arctic, as reported in Dong et al. (2010), where the climatological analysis of 10 years of observations at the ARM NSA site and NOAA Barrow Observatory in Utqiavik, Alaska, suggests an annual Terr-D (Terr-U) of  $240.0$  and  $241.1 \text{ W m}^{-2}$  ( $271.3$  and  $273.1 \text{ W m}^{-2}$ ), respectively (see Fig. 2 in Dong et al. (2010)). In this study, the mean Terr-D for TCARSe2, CERES SYN and MOSAiC observations are  $230.2$ ,  $224.0$  and  $226.5 \text{ W m}^{-2}$ , correspondingly (not shown). The mean Terr-U for TCARSe2, CERES SYN and MOSAiC observations are  $251.0$ ,  $250.7$ , and  $250.2 \text{ W m}^{-2}$ , respectively, leading to a Terr-N at the SFC of  $-20.8$ ,  $-26.7$  and  $-23.7 \text{ W m}^{-2}$  for TCARSe1, CERES SYN and ASFS-30, respectively (Table 6).

The study by Ebell et al. (2020) also presents observations of downwelling terrestrial radiation (Terr-D) from June 2016 to August 2018 for Ny-Ålesund, Svalbard (see Fig. 2 in Ebell et al. (2020)). While the highest values are similarly observed in July and August, consistent with the findings here and in Dong et al. (2010), the minimum Terr-D observed during the Polar Night did not fall below  $200$ . This contrasts with the findings of this study and Dong et al. (2010), where minimum values reached around  $170 \text{ W m}^{-2}$ . The higher values observed at Ny-Ålesund are characteristic of the region, as the location of

the AWIPEV (Alfred Wegener Institute for Polar and Marine Research) Research Base, where the observations were collected, is known for frequent atmospheric advection that transports warm and moist air, unlike other regions in the Arctic (Dahlke and Maturilli, 2017).

The solar flux at the SFC is shown in Figures 6c and 6b. The box plots for TCARSe2 and ASFS-30 exhibit relatively similar patterns across all months. In contrast, the CERES SYN data shows a clear overestimation of the Sol-N flux, primarily due to lower surface albedo values considered in CERES SYN. With an underestimation of surface albedo by -21.01 % (Huang et al., 2022), the even higher solar flux suggests an underestimation of atmospheric opacity, as more radiation is absorbed by the surface based on CERES SYN product. However, it is important to note that the underestimation of cloud opacity is more pronounced during Polar night than during Polar day months (Fig. 7). The Sol-N values for TCARSe2, CERES SYN, and ASFS-30 are 50.2, 74.3, and 46.9  $W m^{-2}$ , respectively, indicating that TCARSe2 provides a better representation of the observed Sol-N flux than the CERES SYN products (Table 6).

The Total flux at the SFC, shows a consistent dominance of the Terr flux for most of the year through March 2020 (Fig. 6e). April is the transition month where the values start to become relatively more positive. From May to August 2020 the Net fluxes at the SFC are dominated by the Sol fluxes. The first 20 days of September 2020, are also part of a transition mode where the Net fluxes are near 0  $W m^{-2}$ . The Total flux at the surface for the MOSAiC period based on TCARS, CERES SYN, and observations are 1.7, 15.6, and 3.9  $W m^{-2}$ . The over-estimation of the Total flux from CERES SYN is driven by the Sol-N by about 27.4  $W m^{-2}$ , whereas the underestimation in the Terr-N accounts for 3.0  $W m^{-2}$ . Using the derived surface albedo from CERES SYN and ShupeTurner retrievals (i.e., TCARSe1) suggests an overall overestimation of the Total flux by 13.9  $W m^{-2}$  (Table 6).

Figure 8a illustrates the monthly Terr-N flux at the TOA, showing a consistent annual variation between TCARSe1 and CERES SYN, indicating less negative values of the outgoing terrestrial radiation during Polar night in contrast to Polar day, as more radiation is emitted from the surface and transmitted through the atmosphere to the TOA due to warmer and more humid conditions. The mean Terr-N for TCARSe1 and CERES SYN is -193.6 and -193.7  $W m^{-2}$ , respectively (Table 6, Fig. 8b).

The comparison of the Sol-N is depicted in panels c and d of Fig. 8. TCARSe2 calculations exhibit a consistent variation compared to CERES SYN calculations, reaching the highest values in July 2020, and then decreasing in magnitude and variability as a result of decreased surface albedo until September 2020. This behaviour is due to the interactions of clouds with a lower surface albedo and lower sun elevations for this period of the year. The mean Sol-N at the TOA for TCARSe2 is 59.7  $W m^{-2}$  whereas, while for CERES SYN, the mean value is 71.8  $W m^{-2}$ , indicating that less solar radiation is absorbed by the atmosphere-surface system in TCARS simulations due to larger atmospheric opacity, which inhibits. This indicates that the surface-atmosphere system in TCARSe2 simulations absorbs more solar radiation due to greater atmospheric opacity. This increased opacity inhibits a significant amount of solar flux from reaching the surface, thus reducing the Sol-U flux resulting in a lower solar flux (Sol-U) reaching the TOA (see Table 6, Fig. 8d).

At the TOA, the radiation budget is predominantly influenced by the Terr flux for the majority of the MOSAiC period, as depicted in Fig. 8e, with the exceptions being June and July. The net radiation at the TOA, calculated using TCARS

and CERES SYN observations, is  $-92.7 \text{ W m}^{-2}$  and  $-105.7 \text{ W m}^{-2}$ , respectively. The discrepancy between these values is primarily attributed to differences in the Sol flux, whereas the Terr fluxes exhibit better agreement.

#### 4.6 Cloud radiative effect

Similarly to Section 4.4, the cloud radiative effect is presented in both monthly and full-year statistics. The calculation of the CRE at the SFC and at the TOA are considers Eq. (1) and is displayed in Fig. 9 and Fig. 10, respectively. The Additionally, the analysis at the SFC considers the hybrid calculation of the CRE by considering the TCARSe2 cloudless simulations and the observations of upwelling and downwelling Sol and Terr fluxes at ASFS-30 (shown in black in Fig. 9).

The distribution of the Terr CRE shows a decrease of the Terr during Polar lower values during polar night and larger values calculated in for October 2019 and from May to September 2020. The annual variation of the Terr CRE is consistent with the findings reported at other sites like the SHEBA (Surface Heat Budget of the Arctic) expedition carried out from 1997 to 1998 north of Alaska (see Fig. 4a in Shupe and Intrieri (2004), Intrieri et al. (2002)), (Intrieri et al., 2002; Shupe and Intrieri, 2004), Ny-Ålesund (see Fig. 6c in Ebell et al. (2020))(Ebell et al., 2020), at the ARM NSA and NOAA Barrow Observatory in Utqiavik (see Fig. 3b in Dong et al. (2010))(Dong et al., 2010), and in Greenland at Summit Station ( $72.68^{\circ}\text{N}$ ,  $38.58^{\circ}\text{W}$ ) (see Fig. 6b in Miller et al. (2015)). (Miller et al., 2015).

Additional attention should be given to September 2020, as the largest CERES SYN discrepancies are found during this month. The Terr-D flux is considerably underestimated (notably underestimated (see Fig. 6a) and does not represent align with the atmospheric opacity indicated by the other datasets (refer to Fig. 7 m).

The biggest difference among the mentioned sites is that the monthly Terr CRE mean at the two Utqiavik sites (Dong et al., 2010) are the lowest in March, with values around  $10 \text{ W m}^{-2}$ , contrasting with the lowest mean values around  $30 \text{ W m}^{-2}$  calculated in this study and at the other sites. These differences stem from the particular characteristics at each site (Shupe et al., 2011). It is important to note that this comparison aims to provide a general context for the observations at other sites rather than a direct comparison, as the data sampling periods and the amount of data considered differ. Additionally, some discrepancies are due to different references for cloudless situations differences in how the equivalent clear sky reference was calculated (Dong et al., 2010).

The calculation of Sol CRE shows a consistent increase in magnitude as there is more solar radiation during June and July 2020 at MOSAiC (Fig. 9c). It is noteworthy that positive values are observed for the hybrid calculations, as broken cloud conditions are not excluded from this analysis. These conditions cannot be simulated within the one-dimensional (1D) radiative transfer setup of TCARS and CERES SYN, hence the values from these models cannot be positive.

Stapf et al. (2020) argued that the calculation of the solar cloud radiative effect should be reassessed by differentiating between the importance distinguishing between the roles of cloudless and all-sky surface albedo. They discuss the applicability of a broadband parameterization that accounts for considers the presence of liquid clouds. However, future research in this area should also consider the influence of ice and mixed-phase clouds, as well as surface conditions such as pond fraction, fresh snow, white snow, melting snow, and their dependency on the Based on aircraft observations, Jäkel et al. (2024) additionally considered the impact of surface type including snow coverage and melt-pond faction, and compared these observations to

the surface albedo scheme of an atmospheric model. Understanding how factors such as surface type, solar zenith angle. A comprehensive investigation into these factors is , and cloud properties including the thermodynamic phase of clouds influences broadband surface albedo is important but beyond the scope of the current work.

At the TOA, the variation of the terrestrial cloud radiative effect (Terr CRE ) CRE is determined by the cloud top temperature relative to the inversion top temperature. A warming effect is associated with high-level clouds, while a cooling effect occurs when the cloud top temperature is similar to the top atmospheric inversion temperature, a condition more common with mid- and low-level clouds. May and June had the highest cloud occurrence during MOSAiC (Fig. 2), resulting in one of the highest mean Terr CRE values at the TOA, around  $10.0 \text{ W m}^{-2}$  (Fig. 10a). The mean Terr CRE for the entire MOSAiC period is  $6.5 \text{ W m}^{-2}$  and  $7.0 \text{ W m}^{-2}$  for TCARSe2 and CERES SYN, respectively.

The Sol CRE at the TOA shows lower values for TCARSe2 in comparison to CERES SYN. The coolest CRE occurs in July with a mean values of  $-51.2$  and  $-67 \text{ W m}^{-2}$  for TCARSe2 and CERES SYN, respectively (Fig. 10b). The mean Sol CRE for the MOSAiC period is  $-26.9 \text{ W m}^{-2}$  for TCARSe2 and  $-34.2 \text{ W m}^{-2}$  for CERES SYN.

The Net CRE Total CREs at the SFC and TOA are shown in Fig. 9e, f and Fig. 10e, f, respectively. The time series shows a dominance of warming CRE at the SFC for most of the months except for July 2020 at the SFC and for June, July, and August 2020 at the TOA. For the entire MOSAiC period, the net Total CRE at the SFC based on TCARS, CERES SYN and hybrid calculations is  $29.3$ ,  $26.4$ , and  $25.0 \text{ W m}^{-2}$ , respectively (Table 6). At the TOA the net Total CRE is dominated by the cooling effect of  $-5.2 \text{ W m}^{-2}$  based on TCARSe2 calculations and of  $-8.5 \text{ W m}^{-2}$  based on CERES SYN (Table 6, Fig. 10e and f). The latter indicates that during MOSAiC, the atmosphere-surface system loses  $5.2 \text{ W m}^{-2}$  to space while the surface gains  $25.0 \text{ W m}^{-2}$  due to the presence of clouds leading to a cooling of the atmosphere by  $30.2 \text{ W m}^{-2}$ .

## 5 Summary, conclusions and outlook

This study investigated analysed the radiation budget and the cloud radiative effect at the surface and the TOA during the MOSAiC expedition. The analysis included an evaluation of the accuracy of cloud macro- and microphysical retrievals based on a combination of accuracy of Shupe-Turner cloud products, based on passive and active remote sensing observations and the ShupeTurner algorithm, was indirectly evaluated through radiative closure studies. These retrievals were utilised served as input parameters for a one-dimensional (1D) single-column radiative transfer model environment (named TCARS), which uses the RRTMG radiative transfer solver to constrain the radiative impact at the surface and TOA to obtain a dataset of simulated radiative flux profiles.

The results from the radiative transfer simulations simulated fluxes were compared to observations of broadband upwelling and downwelling solar and terrestrial radiative fluxes measured at different stations located over the ice floe and collocated satellite products from CERES SYN Ed. 4. Our results indicate that, in general, there is an overall agreement between the performed radiative transfer among the simulations, CERES SYN product data, and ice floe observations making our analysis sufficient to characterise supporting our analysis of the radiation budget and investigate the cloud radiative effect cloud radiative effects during the MOSAiC expedition.

In addition, we evaluated three **versions experiments** of the TCARS simulations by using different **values sources** of surface albedo as input parameters to constrain the **surface-cloud surface-cloud-radiation** interaction and its effect on the Sol-D flux.

Guided by the research questions proposed in the introduction, we summarise our findings and conclude the following:

1. The cloudless TCARS and CERES SYN simulated results exhibit good agreement for Terr and Sol fluxes at both the surface and TOA. The results suggest a consistent correlation across seasons, with correlation coefficients greater than 0.87. However, more notable differences in mean downwelling fluxes are observed for the Sol-D during summer months, displaying a mean flux difference of up to  $7.2 \text{ W m}^{-2}$ . This discrepancy is attributed to **aerosol presence the presence of aerosols**, as a comparison using pristine CERES SYN product reduces the bias to  $-2.0 \text{ W m}^{-2}$ .
2. Overall comparisons between TCARS and MOSAiC flux observations indicate a relatively good agreement for all-sky, cloudy, and cloudless conditions, with median flux differences that do not exceed  $\pm 4.8 \text{ W m}^{-2}$  for the Terr-D and  $\pm 6.8 \text{ W m}^{-2}$  for the Sol-D flux.

The comparison of CERES SYN fluxes to MOSAiC observations also suggests good agreement for Terr-D and Sol-D fluxes, with hourly median flux differences not exceeding  $10.2 \text{ W m}^{-2}$ . However, in contrast to the TCARS results, the CERES SYN comparison displays negative and positive biases for Terr-D and Sol-D fluxes, respectively. This suggests a plausible underestimation of cloud optical thickness, as previously suggested by Huang et al. (2022).

3. Having several ground-based observations of radiative fluxes over the ice floe covering areas of up to approximately 20 km (Cox et al., 2023e) aids the analysis of spatial scale differences between a shipborne measurement and a satellite footprint or grid product. This analysis revealed that the Terr-D flux did not exhibit large variations among Met-City, ASFS-30, ASFS-40, and ASFS-50 observations corroborating the findings in Rabe et al. (2024). On the other hand, other flux components were susceptible to larger differences, especially under cloudless conditions, when the Sol-U fluxes varied by up to  $15 \text{ W m}^{-2}$ . This indicates that the spread among sites was large enough to capture small scale spatiotemporal variability of the surface conditions. Moreover, all of these surface observations were made over sea ice, and thus do not capture the variability of albedo on larger-scales that include some contributions from leads.
4. Evaluating the Net-Terr flux **at the surface** provides an approximation of **the** atmospheric opacity. **During winter, In winter, atmospheric conditions show a bimodal distribution is characteristic of the atmospheric conditions, whereas in summer the atmosphere is characterised , while summer is characterized** by optically thick clouds. **The comparison of Comparing** Net-Terr **aided in identifying periods during which over/under estimations of cloud opacity led to significant biases for helped identify periods when cloud opacity estimates caused biases in TCARS and CERES SYN productproducts.**

**The most significant and recurrent cases in which CERES SYN presented an underestimation of cloud opacity occurred CERES SYN often underestimates cloud opacity during snowfall events. This is more frequent during , particularly in the polar night season. Based on detailed analysis, we suspect that CERES SYN misidentifies , likely due to misidentifying the cloud base by retrieving cloud temperature much with temperatures lower than observed during MOSAiC.**

For TCARS results, overestimation of cloud opacity occurred more frequently during . In contrast, TCARS tends to overestimate cloud opacity with geometrically thick ice clouds. It is plausible that the overestimation of cloud opacity is due to overestimation of the cloud ice water content, which might result from the use of retrieval coefficients that were , possibly due to using retrieval coefficients developed for other Arctic locations (Shupe et al., 2005) and areas (Shupe et al., 2005), which may not be optimal suitable for MOSAiC. Nonetheless, the closure statistics presented here are quite similar to those achieved for a different time period at the NSA site (Shupe et al., 2015), suggesting a general consistency of the ShupeTurner product and the radiative closure framework.

5. The surface radiation budget during MOSAiC indicated a clear dominance of the terrestrial flux for most months with the exception of May, June, July and August. A relatively similar distribution of the Terr-N flux is observed for the TCARS, CERES SYN, and MOSAiC observations with values ranging from -20.8 to -28.3  $\text{W m}^{-2}$ . The mean Sol-N flux for the MOSAiC period ranged from 46.9 to 22.1 to 74.3 34.9  $\text{W m}^{-2}$ . Results of the yearly cycle of the net and downwelling fluxes are comparable to previous results shown in Intrieri et al. (2002), Dong et al. (2010), Miller et al. (2015), and Ebell et al. (2020) for the sites of SHEBA, Summit in Greenland, Alaska, and Ny-Ålesund, respectively.
6. The analysis of the Total CRE at the surface , based on using TCARS, CERES SYN, and a hybrid version using TCARS cloudless simulations and ice-floe observations, indicated relatively approach showed good agreement, suggesting indicating a warming effect of clouds at the surface ranging from between 19.5 to 30.6  $\text{W m}^{-2}$ . Throughout the yearly cycle, there is consistent agreement between TCARS and the hybrid Terr CRE calculation. However, during the polar nightmonths, TCARS suggests larger CRE values possibly attributed to an overestimation of atmospheric opacity of geometrically thick ice clouds year, TCARS and hybrid calculations aligned well, though TCARS showed higher CRE values during polar night, possibly due to overestimating ice cloud opacity from ShupeTurner retrievals. CERES SYN product products have a similar mean and median Terr CRE as the hybrid calculation, but this is likely compensated by a less humid and colder cloudless atmosphere utilised in CERES SYN to simulate the radiative fluxes at the surface. The overall results are within the same range as previous findings described for annual periods in Intrieri et al. (2002); Shupe and Intrieri (2004); Dong et al. (2010); Miller et al. (2015); Ebell et al. (2020), but with slightly different characteristics attributed to the Overall, results were consistent with earlier studies (Intrieri et al., 2002; Shupe a but differed based on unique atmospheric and surface conditions of each site.

Future work should focus on the variation representation and variability of surface albedo across scales. Given the sensitivity of radiative fluxes different scales, as radiative fluxes and cloud radiative effects are sensitive to these influences. It is essential to surface albedo it is important to quantify the spatiotemporal variability from shipborne measurements to satellite footprints, thereby extending the findings presented in this paper and in Huang et al. (2022) . Furthermore, we suggest further analysis of the building on findings from this paper as well as Huang et al. (2022) and Jäkel et al. (2024). We also recommend analysing differences in CERES SYN by utilising using a reanalysis product that assimilates the radiosondes launched during MOSAiC. It is suspected that the incorporates radiosondes from MOSAiC, as GEOS-5.4.1 reanalysis products may represent may reflect

a less humid and , colder Arctic atmosphere during Polar polar night. Lastly, this analysis can be deepened by focusing on the atmospheric processes and the relevance of atmospheric heating rates examined with the radiative transfer simulations generated in this study. Our future plans involve broadening the we aim to deepen the analysis of atmospheric processes related to heating rates, and expand the climatological relevance of these findings by considering other Arctic sites such as including other Arctic locations like Ny-Ålesund.

## 6 Code and data availability

The analysed ShupeTurner cloud macro and microphysical retrievals is publish under Shupe (2022). Ice-floe observations at Met-City and ASFS-30, ASFS-40 and ASFS-50 stations are published in Cox et al. (2023a), Cox et al. (2023b), Cox et al. (2023c), and Cox et al. (2023d), respectively. The data used for surface parameters based on single layer hourly ERA5 data is available at Hersbach et al. (2018b) and for pressure levels is published under Hersbach et al. (2018a). The CERES SYN1deg products were obtained from the NASA Langley Research Center Atmospheric Science Data Center, and are published at NASA/LARC/SD/ASDC (2017). All simulations are currently published on Zenodo as three sets of experiments in monthly files. The radiative transfer simulations are published in Barrientos-Velasco (2024). The TCARS radiative transfer simulations use the Python interface pyRRTMG version 0.9.1 to the RRTMG<sub>LW</sub> and RRTMG<sub>SW</sub> models, which is published under Deneke (2024).

*Author contributions.* CBV, HD, AH, and AM conceptualised the manuscript, HD and AM provided supervision. CBV performed the formal analysis, investigation, data curation, methodology, visualisation and writing of the manuscript. MS and CC contributed to the data curation and validation. HD and AM acquired the funding for this study. All authors contributed to the discussion of the results, subsequent improvement of the analysis, review, and editing of the manuscript.

*Competing interests.* The authors declare that they have no conflict of interest.

*Acknowledgements.* We would like to express our gratitude for the funding provided by the Bundesministerium für Bildung und Forschung for the MOSARiCs project (Combining MOSAiC and Satellite Observations for Radiative Closure and Climate Implications) - Project Number 03F0890A, and the Deutsche Forschungsgemeinschaft (DFG, German Research Foundation) - Project Number 268020496 - TRR 172, within the Transregional Collaborative Research Center "Arctic Amplification: Climate Relevant Atmospheric and Surface Processes, and Feedback Mechanisms (AC)<sup>3</sup>" during phase III. Data used in this manuscript was produced as part of the international Multidisciplinary drifting Observatory for the Study of the Arctic Climate (MOSAiC) with the tag MOSAiC20192020, therefore we are also deeply thankful to the MOSAiC crew and international scientists for their cooperation and collecting invaluable observations. Additionally, we thank the anonymous reviewers for their Aku Riihelä and the anonymous reviewer for their valuable suggestions and comments, which significantly

improved the final version of this manuscript. A subset of data was obtained from the Atmospheric Radiation Measurement (ARM) User Facility, a U.S. Department of Energy (DOE) Office of Science User Facility Managed by the Biological and Environmental Research Program. We would also like to acknowledge the Copernicus Climate Change Service (C3S) for making their ERA5 products easily accessible. Finally, we extend our appreciation to the NASA Langley Research Center Atmospheric Science Data Center for making their products available for the analysis of this study. Cox and Shupe received support from NOAA's Global Ocean Monitoring and Observing Program (FundRef <https://doi.org/10.13039/100018302>) and the NOAA Physical Sciences Laboratory ([NA22OAR4320151](#)). Shupe received additional support from the DOE (DE-SC0021341), National Science Foundation (OPP-1724551), and a Mercator Fellowship with (AC)<sup>3</sup>.

## References

- Atlas, D., Matrosov, S. Y., Heymsfield, A. J., Chou, M.-D., and Wolff, D. B.: Radar and Radiation Properties of Ice Clouds, *Journal of Applied Meteorology and Climatology*, 34, 2329 – 2345, [https://doi.org/https://doi.org/10.1175/1520-0450\(1995\)034<2329:RARPOI>2.0.CO;2](https://doi.org/https://doi.org/10.1175/1520-0450(1995)034<2329:RARPOI>2.0.CO;2), 1995.
- Barker, H. W., Stephens, G. L., Partain, P. T., Bergman, J. W., Bonnel, B., Campana, K., Clothiaux, E. E., Clough, S., Cusack, S., Delamere, J., Edwards, J., Evans, K. F., Fouquart, Y., Freidenreich, S., Galin, V., Hou, Y., Kato, S., Li, J., Mlawer, E., Morcrette, J.-J., O'Hirok, W., Räisänen, P., Ramaswamy, V., Ritter, B., Rozanov, E., Schlesinger, M., Shibata, K., Sporyshev, P., Sun, Z., Wendisch, M., Wood, N., and Yang, F.: Assessing 1D Atmospheric Solar Radiative Transfer Models: Interpretation and Handling of Unresolved Clouds, *Journal of Climate*, 16, 2676–2699, [https://doi.org/10.1175/1520-0442\(2003\)016<2676:ADASRT>2.0.CO;2](https://doi.org/10.1175/1520-0442(2003)016<2676:ADASRT>2.0.CO;2), 2003.
- Barakas, V., Deneke, H., and Macke, A.: The sub-adiabatic model as a concept for evaluating the representation and radiative effects of low-level clouds in a high-resolution atmospheric model, *Atmospheric Chemistry and Physics*, 20, 303–322, <https://doi.org/10.5194/acp-20-303-2020>, 2020.
- Barrientos-Velasco, C.: 1D broadband radiative transfer model simulations for the Multidisciplinary drifting Observatory for the Study of Arctic Climate (MOSAIC) expedition, <https://doi.org/10.5281/zenodo.12514679>, 2024.
- Barrientos Velasco, C., Deneke, H., and Macke, A.: Spatial and temporal variability of broadband solar irradiance during POLARSTERN cruise PS106/1 Ice Floe Camp (June 4th-16th 2017), <https://doi.org/10.1594/PANGAEA.896710>, 2018.
- Barrientos-Velasco, C., Deneke, H., Hünerbein, A., Griesche, H. J., Seifert, P., and Macke, A.: Radiative closure and cloud effects on the radiation budget based on satellite and shipborne observations during the Arctic summer research cruise, PS106, *Atmospheric Chemistry and Physics*, 22, 9313–9348, <https://doi.org/10.5194/acp-22-9313-2022>, 2022.
- Boyer, M., Aliaga, D., Pernov, J. B., Angot, H., Quéléver, L. L. J., Dada, L., Heutte, B., Dall'Osto, M., Beddows, D. C. S., Brasseur, Z., Beck, I., Bucci, S., Duetsch, M., Stohl, A., Laurila, T., Asmi, E., Massling, A., Thomas, D. C., Nøjgaard, J. K., Chan, T., Sharma, S., Tunved, P., Krejci, R., Hansson, H. C., Bianchi, F., Lehtipalo, K., Wiedensohler, A., Weinhold, K., Kulmala, M., Petäjä, T., Sipilä, M., Schmale, J., and Jokinen, T.: A full year of aerosol size distribution data from the central Arctic under an extreme positive Arctic Oscillation: insights from the Multidisciplinary drifting Observatory for the Study of Arctic Climate (MOSAIC) expedition, *Atmospheric Chemistry and Physics*, 23, 389–415, <https://doi.org/10.5194/acp-23-389-2023>, 2023.
- Cadeddu, M. P., Marchand, R., Orlandi, E., Turner, D. D., and Mech, M.: Microwave Passive Ground-Based Retrievals of Cloud and Rain Liquid Water Path in Drizzling Clouds: Challenges and Possibilities, *IEEE Transactions on Geoscience and Remote Sensing*, 55, 6468–6481, <https://doi.org/10.1109/TGRS.2017.2728699>, 2017.
- Cesana, G. V., Pierpaoli, O., Ottaviani, M., Vu, L., Jin, Z., and Silber, I.: The correlation between Arctic sea ice, cloud phase and radiation using A-Train satellites, *Atmospheric Chemistry and Physics*, 24, 7899–7909, <https://doi.org/10.5194/acp-24-7899-2024>, 2024.
- Christensen, M. W., Behrangi, A., L'ecuyer, T. S., Wood, N. B., Lebsock, M. D., and Stephens, G. L.: Arctic Observation and Reanalysis Integrated System: A New Data Product for Validation and Climate Study, *Bulletin of the American Meteorological Society*, 97, 907–916, <https://doi.org/10.1175/BAMS-D-14-00273.1>, 2016.
- Clough, S., Shephard, M., Mlawer, E., Delamere, J., Iacono, M., Cady-Pereira, K., Boukabara, S., and Brown, P.: Atmospheric radiative transfer modeling: a summary of the AER codes, *Journal of Quantitative Spectroscopy and Radiative Transfer*, 91, 233 – 244, <https://doi.org/https://doi.org/10.1016/j.jqsrt.2004.05.058>, 2005.

- Collins, W. D., Rasch, P. J., Eaton, B. E., Khattatov, B. V., Lamarque, J.-F., and Zender, C. S.: Simulating aerosols using a chemical transport model with assimilation of satellite aerosol retrievals: Methodology for INDOEX, *Journal of Geophysical Research: Atmospheres*, 106, 7313–7336, <https://doi.org/10.1029/2000JD900507>, 2001.
- Cox, C., Gallagher, M., Shupe, M., Persson, O., Blomquist, B., Grachev, A., Riihimaki, L., Kutchenreiter, M., Morris, V., Solomon, A., Brooks, I., Costa, D., Gottas, D., Hutchings, J., Osborn, J., Morris, S., Preusser, A., and Uttal, T.: Met City meteorological and surface flux measurements (Level 3 Final), Multidisciplinary Drifting Observatory for the Study of Arctic Climate (MOSAiC), central Arctic, October 2019 - September 2020, Arctic Data Center, <https://doi.org/10.18739/A2PV6B83F>, 2023a.
- Cox, C., Gallagher, M., Shupe, M., Persson, O., Grachev, A., Solomon, A., Ayers, T., Costa, D., Hutchings, J., Leach, J., Morris, S., Osborn, J., Pezoa, S., and Uttal, T.: Atmospheric Surface Flux Station 30 measurements (Level 3 Final), Multidisciplinary Drifting Observatory for the Study of Arctic Climate (MOSAiC), central Arctic, October 2019 - September 2020, Arctic Data Center, <https://doi.org/10.18739/A2FF3M18K>, 2023b.
- Cox, C., Gallagher, M., Shupe, M., Persson, O., Grachev, A., Solomon, A., Ayers, T., Costa, D., Hutchings, J., Leach, J., Morris, S., Osborn, J., Pezoa, S., and Uttal, T.: Atmospheric Surface Flux Station 40 measurements (Level 3 Final), Multidisciplinary Drifting Observatory for the Study of Arctic Climate (MOSAiC), central Arctic, October 2019 - September 2020, Arctic Data Center, <https://doi.org/10.18739/A25X25F0P>, 2023c.
- Cox, C., Gallagher, M., Shupe, M., Persson, O., Grachev, A., Solomon, A., Ayers, T., Costa, D., Hutchings, J., Leach, J., Morris, S., Osborn, J., Pezoa, S., and Uttal, T.: Atmospheric Surface Flux Station 50 measurements (Level 3 Final), Multidisciplinary Drifting Observatory for the Study of Arctic Climate (MOSAiC), central Arctic, October 2019 - September 2020, Arctic Data Center, <https://doi.org/10.18739/A2XD0R00S>, 2023d.
- Cox, C. J., Gallagher, M. R., Shupe, M. D., Persson, P. O. G., Solomon, A., Fairall, C. W., Ayers, T., Blomquist, B., Brooks, I. M., Costa, D., Grachev, A., Gottas, D., Hutchings, J. K., Kutchenreiter, M., Leach, J., Morris, S. M., Morris, V., Osborn, J., Pezoa, S., Preußer, A., Riihimaki, L. D., and Uttal, T.: Continuous observations of the surface energy budget and meteorology over the Arctic sea ice during MOSAiC, *Scientific Data*, 10, <https://doi.org/10.1038/s41597-023-02415-5>, 2023e.
- Dada, L., Angot, H., Beck, I., and et al.: A central arctic extreme aerosol event triggered by a warm air-mass intrusion, *Nat Commun*, 13, 5290, <https://doi.org/10.1038/s41467-022-32872-2>, 2022.
- Dahlke, S. and Maturilli, M.: Contribution of Atmospheric Advection to the Amplified Winter Warming in the Arctic North Atlantic Region, *Advances in Meteorology*, 2017, 1–8, <https://doi.org/10.1155/2017/4928620>, 2017.
- Dahlke, S., Shupe, M. D., Cox, C. J., Brooks, I. M., Blomquist, B., and Persson, P. O. G.: Extended radiosonde profiles 2019/09-2020/10 during MOSAiC Legs PS122/1 - PS122/5, <https://doi.org/10.1594/PANGAEA.961881>, 2023.
- Deneke, H.: hdeneke/pyRRTMG: Release with correct versioning scheme, <https://doi.org/10.5281/zenodo.11147087>, 2024.
- Dong, X., Xi, B., Crosby, K., Long, C. N., Stone, R. S., and Shupe, M. D.: A 10 year climatology of Arctic cloud fraction and radiative forcing at Barrow, Alaska, *Journal of Geophysical Research: Atmospheres*, 115, <https://doi.org/https://doi.org/10.1029/2009JD013489>, 2010.
- Dong, X., Xi, B., Qiu, S., Minnis, P., Sun-Mack, S., and Rose, F.: A radiation closure study of Arctic stratus cloud microphysical properties using the collocated satellite-surface data and Fu-Liou radiative transfer model, *Journal of Geophysical Research: Atmospheres*, 121, 10,175–10,198, <https://doi.org/10.1002/2016JD025255>, 2016.
- Duncan, B. N., Ott, L. E., Abshire, J. B., Brucker, L., Carroll, M. L., Carton, J., Comiso, J. C., Dinnat, E. P., Forbes, B. C., Gonsamo, A., Gregg, W. W., Hall, D. K., Ialongo, I., Jandt, R., Kahn, R. A., Karpechko, A., Kawa, S. R., Kato, S., Kumpula, T., Kyrölä, E., Loboda,

- T. V., McDonald, K. C., Montesano, P. M., Nassar, R., Neigh, C. S., Parkinson, C. L., Poulter, B., Pulliainen, J., Rautiainen, K., Rogers, B. M., Rousseaux, C. S., Soja, A. J., Steiner, N., Tamminen, J., Taylor, P. C., Tzortziou, M. A., Virta, H., Wang, J. S., Watts, J. D., Winker, D. M., and Wu, D. L.: Space-Based Observations for Understanding Changes in the Arctic-Boreal Zone, *Reviews of Geophysics*, 58, e2019RG000652, <https://doi.org/https://doi.org/10.1029/2019RG000652>, e2019RG000652 2019RG000652, 2020.
- Dunn, M., Johnson, K., and Jensen, M.: The Microbase Value-Added Product: A Baseline Retrieval of Cloud Microphysical Properties, <https://doi.org/10.2172/1015189>, 2011.
- Dutton, G., Hall, B., Dlugokencky, E., Lan, X., Nance, J., and Madronich, M.: Combined Atmospheric Nitrous Oxide Dry Air Mole Fractions from the NOAA GML Halocarbons Sampling Network, 1977-2023, version: 2023-04-13, <https://doi.org/10.15138/GMZ7-2Q16>, 2023a.
- Dutton, G., Hall, B., Montzka, S., and Nance, J.: Combined Atmospheric Carbon Tetrachloride Dry Air Mole Fractions from the NOAA GML Halocarbons Sampling Network, 1995-2023, version: 2023-04-13, <https://doi.org/10.15138/CV0A-J604>, 2023b.
- Dutton, G., Hall, S., Montzka, J., and Nance, J.: Combined Atmospheric Chlorofluorocarbon-12 Dry Air Mole Fractions from the NOAA GML Halocarbon Sampling Network, 1977-2023, version: 2023-04-13, <https://doi.org/10.15138/PJ63-H440>, 2023c.
- Dutton, G., Hall, S., Montzka, J. D., and Nance, J.: Combined Atmospheric Chlorofluorocarbon-11 Dry Air Mole Fractions from the NOAA GML Halocarbons Sampling Network, 1977-2023, version: 2023-04-13, <https://doi.org/10.15138/BVQ6-2S69>, 2023d.
- Eastman, R. and Warren, S. G.: Arctic Cloud Changes from Surface and Satellite Observations, *Journal of Climate*, 23, 4233 – 4242, <https://doi.org/https://doi.org/10.1175/2010JCLI3544.1>, 2010.
- Ebell, K., Nomokonova, T., Maturilli, M., and Ritter, C.: Radiative Effect of Clouds at Ny-Ålesund, Svalbard, as Inferred from Ground-Based Remote Sensing Observations, *Journal of Applied Meteorology and Climatology*, 59, 3–22, <https://doi.org/10.1175/JAMC-D-19-0080.1>, 2020.
- Ebell, K., Walbröl, A., Engelmann, R., Griesche, H., Radenz, M., Hofer, J., and Althausen, D.: Temperature and humidity profiles, integrated water vapour and liquid water path derived from the HATPRO microwave radiometer onboard the Polarstern during the MOSAiC expedition, <https://doi.org/10.1594/PANGAEA.941389>, 2022.
- Fu, Q. and Liou, K. N.: On the Correlated k-Distribution Method for Radiative Transfer in Nonhomogeneous Atmospheres, *Journal of the Atmospheric Sciences*, 49, 2139–2156, [https://doi.org/10.1175/1520-0469\(1992\)049<2139:OTCDMF>2.0.CO;2](https://doi.org/10.1175/1520-0469(1992)049<2139:OTCDMF>2.0.CO;2), 1992.
- Fu, Q. and Liou, K. N.: Parameterization of the Radiative Properties of Cirrus Clouds, *Journal of Atmospheric Sciences*, 50, 2008 – 2025, [https://doi.org/https://doi.org/10.1175/1520-0469\(1993\)050<2008:POTRPO>2.0.CO;2](https://doi.org/https://doi.org/10.1175/1520-0469(1993)050<2008:POTRPO>2.0.CO;2), 1993.
- Fu, Q., Lesins, G., Higgins, J., Charlock, T., Chylek, P., and Michalsky, J.: Broadband water vapor absorption of solar radiation tested using ARM data, *Geophysical Research Letters*, 25, 1169–1172, <https://doi.org/https://doi.org/10.1029/98GL00846>, 1998.
- Griesche, H. J., Barrientos-Velasco, C., Deneke, H., Hünerbein, A., Seifert, P., and Macke, A.: Low-level Arctic clouds: A blind zone in our knowledge of the radiation budget, *EGUsphere*, 2023, 1–21, <https://doi.org/10.5194/egusphere-2023-358>, 2023.
- Griesche, H. J., Seifert, P., Engelmann, R., Radenz, M., Hofer, J., Althausen, D., Walbröl, A., Barrientos-Velasco, C., Baars, H., Dahlke, S., Tukiainen, S., and Macke, A.: Cloud micro- and macrophysical properties from ground-based remote sensing during the MOSAiC drift experiment, *Scientific Data*, 11, 505, <https://doi.org/10.1038/s41597-024-03325-w>, 2024.
- Gu, B.: Evaluations and Improvements of the RRTMG and Fu-Liou Radiative Transfer Model Simulations of Clouds, Doctoral dissertation, Texas A&M University, available electronically from <https://hdl.handle.net/1969.1/189047>, 2019.
- Gupta, S. K., Kratz, D. P., Stackhouse, Paul W., J., Wilber, A. C., Zhang, T., and Sothcott, V. E.: Improvement of Surface Longwave Flux Algorithms Used in CERES Processing, *Journal of Applied Meteorology and Climatology*, 49, 1579–1589, <https://doi.org/10.1175/2010JAMC2463.1>, 2010.

- Guzman, R., Chepfer, H., Noel, V., Vaillant de Guélis, T., Kay, J. E., Raberanto, P., Cesana, G., Vaughan, M. A., and Winker, D. M.: Direct atmosphere opacity observations from CALIPSO provide new constraints on cloud-radiation interactions, *Journal of Geophysical Research: Atmospheres*, 122, 1066–1085, <https://doi.org/https://doi.org/10.1002/2016JD025946>, 2017.
- Hartmann, D. L. and Ceppi, P.: Trends in the CERES Dataset, 2000–13: The Effects of Sea Ice and Jet Shifts and Comparison to Climate Models, *Journal of Climate*, 27, 2444 – 2456, <https://doi.org/10.1175/JCLI-D-13-00411.1>, 2014.
- Heinemann, G., Schefczyk, L., Zentek, R., Brooks, I. M., Dahlke, S., and Walbröl, A.: Evaluation of Vertical Profiles and Atmospheric Boundary Layer Structure Using the Regional Climate Model CCLM during MOSAiC, *Meteorology*, 2, 257–275, <https://doi.org/10.3390/meteorology2020016>, 2023.
- Herrmannsdörfer, L., Müller, M., Shupe, M. D., and Rostosky, P.: Surface temperature comparison of the Arctic winter MOSAiC observations, ERA5 reanalysis, and MODIS satellite retrieval, *Elementa: Science of the Anthropocene*, 11, 00085, <https://doi.org/10.1525/elementa.2022.00085>, 2023.
- Hersbach, H., Bell, B., Berrisford, P., Biavati, G., Horányi, A., Muñoz Sabater, J., Nicolas, J., Peubey, C., Radu, R., Rozum, I., Schepers, D., Simmons, A., Soci, C., Dee, D., and Thépaut, J.-N.: ERA5 hourly data on pressure levels from 1979 to present. Copernicus Climate Change Service (C3S) Climate Data Store (CDS), <https://doi.org/10.24381/cds.bd0915c6>, accessed on: 02/07/2020, 2018a.
- Hersbach, H., Bell, B., Berrisford, P., Biavati, G., Horányi, A., Muñoz Sabater, J., Nicolas, J., Peubey, C., Radu, R., Rozum, I., Schepers, D., Simmons, A., Soci, C., Dee, D., and Thépaut, J.-N.: ERA5 hourly data on single levels from 1979 to present. Copernicus Climate Change Service (C3S) Climate Data Store (CDS), <https://doi.org/10.24381/cds.adbb2d47>, accessed on: 17/04/2020, 2018b.
- Hersbach, H., Bell, B., Berrisford, P., Hirahara, S., Horányi, A., Muñoz-Sabater, J., Nicolas, J., Peubey, C., Radu, R., Schepers, D., Simmons, A., Soci, C., Abdalla, S., Abellan, X., Balsamo, G., Bechtold, P., Biavati, G., Bidlot, J., Bonavita, M., De Chiara, G., Dahlgren, P., Dee, D., Diamantakis, M., Dragani, R., Flemming, J., Forbes, R., Fuentes, M., Geer, A., Haimberger, L., Healy, S., Hogan, R. J., Hólm, E., Janisková, M., Keeley, S., Laloyaux, P., Lopez, P., Lupu, C., Radnoti, G., de Rosnay, P., Rozum, I., Vamborg, F., Villaume, S., and Thépaut, J.-N.: The ERA5 global reanalysis, *Quarterly Journal of the Royal Meteorological Society*, 146, 1999–2049, <https://doi.org/https://doi.org/10.1002/qj.3803>, 2020.
- Hu, Y. X. and Stamnes, K.: An Accurate Parameterization of the Radiative Properties of Water Clouds Suitable for Use in Climate Models, *Journal of Climate*, 6, 728–742, [https://doi.org/10.1175/1520-0442\(1993\)006<0728:AAPOTR>2.0.CO;2](https://doi.org/10.1175/1520-0442(1993)006<0728:AAPOTR>2.0.CO;2), 1993.
- Huang, Y., Dong, X., Xi, B., Dolinar, E. K., Stanfield, R. E., and Qiu, S.: Quantifying the Uncertainties of Reanalyzed Arctic Cloud and Radiation Properties Using Satellite Surface Observations, *Journal of Climate*, 30, 8007–8029, <https://doi.org/10.1175/JCLI-D-16-0722.1>, 2017.
- Huang, Y., Taylor, P. C., Rose, F. G., Rutan, D. A., Shupe, M. D., Webster, M. A., and Smith, M. M.: Toward a more realistic representation of surface albedo in NASA CERES-derived surface radiative fluxes: A comparison with the MOSAiC field campaign: Comparison of CERES and MOSAiC surface radiation fluxes, *Elementa: Science of the Anthropocene*, 10, 00013, <https://doi.org/10.1525/elementa.2022.00013>, 2022.
- Intrieri, J. M., Fairall, C. W., Shupe, M. D., Persson, P. O. G., Andreas, E. L., Guest, P. S., and Moritz, R. E.: An annual cycle of Arctic surface cloud forcing at SHEBA, *Journal of Geophysical Research: Oceans*, 107, SHE 13–1–SHE 13–14, <https://doi.org/10.1029/2000JC000439>, 2002.
- Jäkel, E., Becker, S., Sperzel, T. R., Niehaus, H., Spreen, G., Tao, R., Nicolaus, M., Dorn, W., Rinke, A., Brauchle, J., and Wendisch, M.: Observations and modeling of areal surface albedo and surface types in the Arctic, *The Cryosphere*, 18, 1185–1205, <https://doi.org/10.5194/tc-18-1185-2024>, 2024.

- Jensen, M., Giangrande, S., Fairless, T., and Zhou, A.: interpolatedsonde, <https://doi.org/10.5439/1095316>, 1998.
- Jin, Z., Charlock, T. P., Smith Jr., W. L., and Rutledge, K.: A parameterization of ocean surface albedo, *Geophysical Research Letters*, 31, <https://doi.org/https://doi.org/10.1029/2004GL021180>, 2004.
- Johnson, K., Giangrande, S., and Toto, T.: KAZRARASCL-c0-All-inclusive data stream, <https://doi.org/10.5439/1393437>, 2014.
- Jozef, G. C., Cassano, J. J., Dahlke, S., Dice, M., Cox, C. J., and de Boer, G.: Thermodynamic and Kinematic Drivers of Atmospheric Boundary Layer Stability in the Central Arctic during MOSAiC, *EGUosphere*, 2023, 1–28, <https://doi.org/10.5194/egusphere-2023-824>, 2023.
- Kato, S., Ackerman, T. P., Mather, J. H., and Clothiaux, E. E.: The k-distribution method and correlated-k approximation for a shortwave radiative transfer model, *Journal of Quantitative Spectroscopy and Radiative Transfer*, 62, 109–121, [https://doi.org/https://doi.org/10.1016/S0022-4073\(98\)00075-2](https://doi.org/https://doi.org/10.1016/S0022-4073(98)00075-2), 1999.
- Kato, S., Rose, F. G., and Charlock, T. P.: Computation of Domain-Averaged Irradiance Using Satellite-Derived Cloud Properties, *Journal of Atmospheric and Oceanic Technology*, 22, 146 – 164, <https://doi.org/https://doi.org/10.1175/JTECH-1694.1>, 2005.
- Kato, S., Loeb, N. G., Rutan, D. A., et al.: Uncertainty Estimate of Surface Irradiances Computed with MODIS-, CALIPSO-, and CloudSat-Derived Cloud and Aerosol Properties, *Surveys in Geophysics*, 33, 395–412, <https://doi.org/10.1007/s10712-012-9179-x>, 2012.
- Kato, S., Rose, F. G., Rutan, D. A., Thorsen, T. J., Loeb, N. G., Doelling, D. R., Huang, X., Smith, W. L., Su, W., and Ham, S.-H.: Surface Irradiances of Edition 4.0 Clouds and the Earth’s Radiant Energy System (CERES) Energy Balanced and Filled (EBAF) Data Product, *Journal of Climate*, 31, 4501–4527, <https://doi.org/10.1175/JCLI-D-17-0523.1>, 2018.
- Kay, J. E., L’Ecuyer, T., Chepfer, H., Loeb, N., Morrison, A., and Cesana, G.: Recent Advances in Arctic Cloud and Climate Research, *Current Climate Change Reports*, 2, 159–169, <https://doi.org/10.1007/s40641-016-0051-9>, 2016.
- Key, J.: Streamer user’s guide., Tech. Rep., pp. 96–01, 85, <https://geocryos.ssec.wisc.edu/streamer/userman.pdf>, last access: 15/07/2022, 1996.
- Kirbus, B., Tiedeck, S., Camplani, A., Chylik, J., Crewell, S., Dahlke, S., Ebell, K., Gorodetskaya, I., Griesche, H., Handorf, D., Höschel, I., Lauer, M., Neggers, R., Rückert, J., Shupe, M. D., Spreen, G., Walbröl, A., Wendisch, M., and Rinke, A.: Surface impacts and associated mechanisms of a moisture intrusion into the Arctic observed in mid-April 2020 during MOSAiC, *Frontiers in Earth Science*, 11, <https://doi.org/10.3389/feart.2023.1147848>, 2023.
- Kratz, D. P. and Rose, F. G.: Accounting for Molecular Absorption Within the Spectral Range of the CERES Window Channel, *Journal of Quantitative Spectroscopy and Radiative Transfer*, 61, 83–95, [https://doi.org/https://doi.org/10.1016/S0022-4073\(97\)00203-3](https://doi.org/https://doi.org/10.1016/S0022-4073(97)00203-3), 1999.
- Kruppen, T., von Albedyll, L., Goessling, H., Hendricks, S., Juhls, B., Spreen, G., Willmes, S., Bünger, H. J., Dethloff, K., Haas, C., Kaleschke, L., Katlein, C., Tian-Kunze, X., Ricker, R., Rostosky, P., Rückert, J., Singha, S., and Sokolova, J.: MOSAiC drift expedition from October 2019 to July 2020: Sea ice conditions from space and comparison with previous years, *The Cryosphere*, 15, 3897–3920, <https://doi.org/10.5194/tc-15-3897-2021>, 2021.
- Lan, X., Dlugokencky, E., Mund, J., Crotwell, A., Crotwell, M., Moglia, E., Madronich, M., Neff, D., and Thoning, K.: Atmospheric Carbon Dioxide Dry Air Mole Fractions from the NOAA GML Carbon Cycle Cooperative Global Air Sampling Network, 1968–2021, version: 2022-11-21, <https://doi.org/10.15138/wkgj-f215>, 2022a.
- Lan, X., Dlugokencky, E., Mund, J., Crotwell, A., Crotwell, M., Moglia, E., Madronich, M., Neff, D., and Thoning, K.: Atmospheric Methane Dry Air Mole Fractions from the NOAA GML Carbon Cycle Cooperative Global Air Sampling Network, 1983–2021, version: 2022-11-21, <https://doi.org/10.15138/VNCZ-M766>, 2022b.

- Lanconelli, C., Busetto, M., Dutton, E. G., König-Langlo, G., Maturilli, M., Sieger, R., Vitale, V., and Yamanouchi, T.: Polar baseline surface radiation measurements during the International Polar Year 2007–2009, *Earth System Science Data*, 3, 1–8, <https://doi.org/10.5194/essd-3-1-2011>, 2011.
- Lawrence, Z. D., Perlwitz, J., Butler, A. H., Manney, G. L., Newman, P. A., Lee, S. H., and Nash, E. R.: The Remarkably Strong Arctic Stratospheric Polar Vortex of Winter 2020: Links to Record-Breaking Arctic Oscillation and Ozone Loss, *Journal of Geophysical Research: Atmospheres*, 125, e2020JD033271, <https://doi.org/10.1029/2020JD033271>, e2020JD033271 10.1029/2020JD033271, 2020.
- Lelli, L., Vountas, M., Khosravi, N., and Burrows, J. P.: Satellite remote sensing of regional and seasonal Arctic cooling showing a multi-decadal trend towards brighter and more liquid clouds, *Atmospheric Chemistry and Physics*, 23, 2579–2611, <https://doi.org/10.5194/acp-23-2579-2023>, 2023.
- Light, B., Smith, M., Perovich, D., Webster, M., Holland, M., Linhardt, F., Raphael, I., Clemens-Sewall, D., Macfarlane, A., Anhaus, P., and Bailey, D.: Arctic sea ice albedo: Spectral composition, spatial heterogeneity, and temporal evolution observed during the MOSAiC drift, *Elementa: Science of the Anthropocene*, 10, <https://doi.org/10.1525/elementa.2021.000103>, 2022.
- Loeb, N. G., Doelling, D. R., Wang, H., Su, W., Nguyen, C., Corbett, J. G., Liang, L., Mitrescu, C., Rose, F. G., and Kato, S.: Clouds and the Earth’s Radiant Energy System (CERES) Energy Balanced and Filled (EBAF) Top-of-Atmosphere (TOA) Edition-4.0 Data Product, *Journal of Climate*, 31, 895 – 918, <https://doi.org/10.1175/JCLI-D-17-0208.1>, 2018.
- López-García, V., Neely, Ryan R., I., Dahlke, S., and Brooks, I. M.: Low-level jets over the Arctic Ocean during MOSAiC, *Elementa: Science of the Anthropocene*, 10, 00063, <https://doi.org/10.1525/elementa.2022.00063>, 2022.
- Mace, G. G., Benson, S., and Kato, S.: Cloud radiative forcing at the Atmospheric Radiation Measurement Program Climate Research Facility: 2. Vertical redistribution of radiant energy by clouds, *Journal of Geophysical Research: Atmospheres*, 111, <https://doi.org/10.1029/2005JD005922>, 2006.
- Macke, A. and Flores, H.: The Expeditions PS106/1 and 2 of the Research Vessel POLARSTERN to the Arctic Ocean in 2017, *Berichte zur Polar- und Meeresforschung*, 714, [https://doi.org/10.2312/BzPM\\_0714\\_2017](https://doi.org/10.2312/BzPM_0714_2017), last access: 13/07/2022, 2018.
- Maturilli, M., Holdridge, D. J., Dahlke, S., Graeser, J., Sommerfeld, A., Jaiser, R., Deckelmann, H., and Schulz, A.: Initial radiosonde data from 2019-10 to 2020-09 during project MOSAiC, <https://doi.org/10.1594/PANGAEA.928656>, 2021.
- Meredith, M., Sommerkorn, M., Cassotta, S., Derksen, C., Ekaykin, A., Hollowed, A., Kofinas, G., Mackintosh, A., Melbourne-Thomas, J., Muelbert, M., Ottersen, G., Pritchard, H., and Schuur, E.: Polar Regions. In: IPCC Special Report on the Ocean and Cryosphere in a Changing Climate, [H.-O. Pörtner, D.C. Roberts, V. Masson-Delmotte, P. Zhai, M. Tignor, E. Poloczanska, K. Mintenbeck, A. Alegría, M. Nicolai, A. Okem, J. Petzold, B. Rama, N.M. Weyer (eds.)]In press., <https://www.ipcc.ch/srocc/chapter/chapter-3-2/>, last access: 13/07/2022, 2019.
- Miller, M. A., Nitschke, K., Ackerman, T. P., Ferrell, W. R., Hickmon, N., and Ivey, M.: The ARM Mobile Facilities, *Meteorological Monographs*, 57, 9.1 – 9.15, <https://doi.org/10.1175/AMSMONOGRAPHS-D-15-0051.1>, 2016.
- Miller, N. B., Shupe, M. D., Cox, C. J., Walden, V. P., Turner, D. D., and Steffen, K.: Cloud Radiative Forcing at Summit, Greenland, *Journal of Climate*, 28, 6267–6280, <https://doi.org/10.1175/JCLI-D-15-0076.1>, 2015.
- Minnis, P., Sun-Mack, S., Chen, Y., Chang, F., Yost, C. R., Smith, W. L., Heck, P. W., Arduini, R. F., Bedka, S. T., Yi, Y., Hong, G., Jin, Z., Painemal, D., Palikonda, R., Scarino, B. R., Spangenberg, D. A., Smith, R. A., Trepte, Q. Z., Yang, P., and Xie, Y.: CERES MODIS Cloud Product Retrievals for Edition 4–Part I: Algorithm Changes, *IEEE Transactions on Geoscience and Remote Sensing*, 59, 2744–2780, <https://doi.org/10.1109/TGRS.2020.3008866>, 2021.

- Mlawer, E. J., Taubman, S. J., Brown, P. D., Iacono, M. J., and Clough, S. A.: Radiative transfer for inhomogeneous atmospheres: RRTM, a validated correlated-k model for the longwave, *Journal of Geophysical Research: Atmospheres*, 102, 16 663–16 682, <https://doi.org/10.1029/97JD00237>, 1997.
- Montzka, S.: HCFCs, Halons, Methyl Chloroform, HFC-134a and HFC-152a, <https://gml.noaa.gov/hats/data.html>, data for individual chemicals can be found at the associated links., 2024.
- Morris, V., Zhang, D., and Ermold, B.: ceil, <https://doi.org/10.5439/1181954>, 1996.
- Morrison, H., de Boer, G., Feingold, G., Harrington, J., Shupe, M. D., and Sulia, K.: Resilience of persistent Arctic mixed-phase clouds, *Nature Geoscience*, 5, 11–17, <https://doi.org/10.1038/ngeo1332>, 2012.
- Murray-Watson, R. J., Gryspeerdt, E., and Goren, T.: Investigating the development of clouds within marine cold-air outbreaks, *Atmospheric Chemistry and Physics*, 23, 9365–9383, <https://doi.org/10.5194/acp-23-9365-2023>, 2023.
- NASA/LARC/SD/ASDC: CERES and GEO-Enhanced TOA, Within-Atmosphere and Surface Fluxes, Clouds and Aerosols 1-Hourly Terra-Aqua Edition4A, [https://doi.org/10.5067/TERRA+AQUA/CERES/SYN1DEG-1HOUR\\_L3.004A](https://doi.org/10.5067/TERRA+AQUA/CERES/SYN1DEG-1HOUR_L3.004A), 2017.
- Nicolaus, M., Perovich, D. K., Spreen, G., Granskog, M. A., von Albedyll, L., Angelopoulos, M., Anhaus, P., Arndt, S., Belter, H. J., Bessonov, V., Birnbaum, G., Brauchle, J., Calmer, R., Cardellach, E., Cheng, B., Clemens-Sewall, D., Dadic, R., Damm, E., de Boer, G., Demir, O., Dethloff, K., Divine, D. V., Fong, A. A., Fons, S., Frey, M. M., Fuchs, N., Gabarró, C., Gerland, S., Goessling, H. F., Gradinger, R., Haapala, J., Haas, C., Hamilton, J., Hannula, H.-R., Hendricks, S., Herber, A., Heuzé, C., Hoppmann, M., Høyland, K. V., Huntemann, M., Hutchings, J. K., Hwang, B., Itkin, P., Jacobi, H.-W., Jaggi, M., Jutila, A., Kaleschke, L., Katlein, C., Kolabutin, N., Krampe, D., Kristensen, S. S., Krumpfen, T., Kurtz, N., Lampert, A., Lange, B. A., Lei, R., Light, B., Linhardt, F., Liston, G. E., Loose, B., Macfarlane, A. R., Mahmud, M., Matero, I. O., Maus, S., Morgenstern, A., Naderpour, R., Nandan, V., Niubom, A., Oggier, M., Oppelt, N., Pätzold, F., Perron, C., Petrovsky, T., Pirazzini, R., Polashenski, C., Rabe, B., Raphael, I. A., Regnery, J., Rex, M., Ricker, R., Riemann-Campe, K., Rinke, A., Rohde, J., Salganik, E., Scharien, R. K., Schiller, M., Schneebeil, M., Semmling, M., Shimanchuk, E., Shupe, M. D., Smith, M. M., Smolyanitsky, V., Sokolov, V., Stanton, T., Stroeve, J., Thielke, L., Timofeeva, A., Tonboe, R. T., Tavri, A., Tsamados, M., Wagner, D. N., Watkins, D., Webster, M., and Wendisch, M.: Overview of the MOSAiC expedition: Snow and sea ice, *Elementa: Science of the Anthropocene*, 10, 000 046, <https://doi.org/10.1525/elementa.2021.000046>, 2022.
- NOAA-AGGI: Global Monitoring Laboratory, National Oceanic and Atmospheric Administration (NOAA), <https://gml.noaa.gov/aggi/aggi.html>, last access: 01/03/2024, 2024.
- Pithan, F., Athanase, M., Dahlke, S., Sánchez-Benítez, A., Shupe, M. D., Sledd, A., Streffing, J., Svensson, G., and Jung, T.: Nudging allows direct evaluation of coupled climate models with in situ observations: a case study from the MOSAiC expedition, *Geoscientific Model Development*, 16, 1857–1873, <https://doi.org/10.5194/gmd-16-1857-2023>, 2023.
- Rabe, B., Heuzé, C., Regnery, J., Aksenov, Y., Allerholt, J., Athanase, M., Bai, Y., Basque, C., Bauch, D., Baumann, T. M., Chen, D., Cole, S. T., Craw, L., Davies, A., Damm, E., Dethloff, K., Divine, D. V., Doglioni, F., Ebert, F., Fang, Y.-C., Fer, I., Fong, A. A., Gradinger, R., Granskog, M. A., Graupner, R., Haas, C., He, H., He, Y., Hoppmann, M., Janout, M., Kadko, D., Kanzow, T., Karam, S., Kawaguchi, Y., Koenig, Z., Kong, B., Krishfield, R. A., Krumpfen, T., Kuhlmeier, D., Kuznetsov, I., Lan, M., Laukert, G., Lei, R., Li, T., Torres-Valdés, S., Lin, L., Lin, L., Liu, H., Liu, N., Loose, B., Ma, X., McKay, R., Mallet, M., Mallett, R. D. C., Maslowski, W., Mertens, C., Mohrholz, V., Muilwijk, M., Nicolaus, M., O'Brien, J. K., Perovich, D., Ren, J., Rex, M., Ribeiro, N., Rinke, A., Schaffer, J., Schuffenhauer, I., Schulz, K., Shupe, M. D., Shaw, W., Sokolov, V., Sommerfeld, A., Spreen, G., Stanton, T., Stephens, M., Su, J., Sukhikh, N., Sundfjord, A., Thomisch, K., Tippenhauer, S., Toole, J. M., Vredenburg, M., Walter, M., Wang, H., Wang, L., Wang, Y., Wendisch, M., Zhao, J.,

- Zhou, M., and Zhu, J.: Overview of the MOSAiC expedition: Physical oceanography, *Elementa: Science of the Anthropocene*, 10, 00062, <https://doi.org/10.1525/elementa.2021.00062>, 2022.
- Rabe, B., Cox, C. J., Fang, Y.-C., Goessling, H., Granskog, M. A., Hoppmann, M., Hutchings, J. K., Krumpfen, T., Kuznetsov, I., Lei, R., Li, T., Maslowski, W., Nicolaus, M., Perovich, D., Persson, O., Regnery, J., Rigor, I., Shupe, M. D., Sokolov, V., Spreen, G., Stanton, T., Watkins, D. M., Blockley, E., Buenger, H. J., Cole, S., Fong, A., Haapala, J., Heuzé, C., Hoppe, C. J. M., Janout, M., Jutila, A., Katlein, C., Krishfield, R., Lin, L., Ludwig, V., Morgenstern, A., O'Brien, J., Zurita, A. Q., Rackow, T., Riemann-Campe, K., Rohde, J., Shaw, W., Smolyanitsky, V., Solomon, A., Sperling, A., Tao, R., Toole, J., Tsamados, M., Zhu, J., and Zuo, G.: The MOSAiC Distributed Network: Observing the coupled Arctic system with multidisciplinary, coordinated platforms, *Elementa: Science of the Anthropocene*, 12, 00103, <https://doi.org/10.1525/elementa.2023.00103>, 2024.
- Rienecker, M. M. . C.: The GOES-5 data assimilation system—documentation of Versions 5.0.1, 5.1.0, and 5.2.0. NASA Tech. Rep. Series on Global Modeling and Data Assimilation NASA/TM-2008-104606, <https://ntrs.nasa.gov/citations/20120011955>, 2008.
- Riihelä, A., Key, J. R., Meirink, J. F., Kuipers Munneke, P., Palo, T., and Karlsson, K.-G.: An intercomparison and validation of satellite-based surface radiative energy flux estimates over the Arctic, *Journal of Geophysical Research: Atmospheres*, 122, 4829–4848, <https://doi.org/10.1002/2016JD026443>, 2017.
- Riihimäki, L. D., Cronin, M. F., Acharya, R., Anderson, N., Augustine, J., Balmes, K. A., Berk, P., Bozzano, R., Bucholtz, A., Connell, K. J., Cox, C., Di Sarra, A. G., James, E. B., Fairall, C., Farrar, J. T., Grissom, K., Guerra, M. T., Hormann, V., Joseph, K. J., Lanconelli, C., Melin, F., Meloni, D., Ottaviani, M., Pensieri, S., Ramesh, K., Rutan, D., Samarinas, N., Smith, S. R., Swart, S., Tandon, A., Venkatesan, R., Thompson, E., Verma, R. K., Watkins-Brandt, K. S., Weller, R. A., Zappa, C. J., and Zhang, D.: Ocean Surface Radiation Measurement Best Practices, *Frontiers*, <https://doi.org/10.3389/fmars.2024.1359149>, 2024.
- Rinke, A., Cassano, J. J., Cassano, E. N., Jaiser, R., and Handorf, D.: Meteorological conditions during the MOSAiC expedition: Normal or anomalous?, *Elementa: Science of the Anthropocene*, 9, 00023, <https://doi.org/10.1525/elementa.2021.00023>, 2021.
- Rose, F. G., Rutan, D. A., Charlock, T., Smith, G. L., and Kato, S.: An Algorithm for the Constraining of Radiative Transfer Calculations to CERES-Observed Broadband Top-of-Atmosphere Irradiance, *Journal of Atmospheric and Oceanic Technology*, 30, 1091–1106, <https://doi.org/10.1175/JTECH-D-12-00058.1>, 2013.
- Rossow, W. B. and Zhang, Y.-C.: Calculation of surface and top of atmosphere radiative fluxes from physical quantities based on ISCCP data sets: 2. Validation and first results, *Journal of Geophysical Research: Atmospheres*, 100, 1167–1197, <https://doi.org/https://doi.org/10.1029/94JD02746>, 1995.
- Rutan, D. A., Kato, S., Doelling, D. R., Rose, F. G., Nguyen, L. T., Caldwell, T. E., and Loeb, N. G.: CERES Synoptic Product: Methodology and Validation of Surface Radiant Flux, *Journal of Atmospheric and Oceanic Technology*, 32, 1121–1143, <https://doi.org/10.1175/JTECH-D-14-00165.1>, 2015.
- Rückert, J. E., Rostosky, P., Huntemann, M., Clemens-Sewall, D., Ebell, K., Kaleschke, L., Lemmetyinen, J., Macfarlane, A. R., Naderpour, R., Stroeve, J., Walbröl, A., and Spreen, G.: Sea ice concentration satellite retrievals influenced by surface changes due to warm air intrusions: A case study from the MOSAiC expedition, *Elementa: Science of the Anthropocene*, 11, 00039, <https://doi.org/10.1525/elementa.2023.00039>, 2023.
- Sassen, K.: Ice Cloud Content from Radar Reflectivity, *Journal of Applied Meteorology and Climatology*, 26, 1050 – 1053, [https://doi.org/https://doi.org/10.1175/1520-0450\(1987\)026<1050:ICCFRR>2.0.CO;2](https://doi.org/https://doi.org/10.1175/1520-0450(1987)026<1050:ICCFRR>2.0.CO;2), 1987.
- Serreze, M. C. and Barry, R. G.: Processes and impacts of Arctic amplification: A research synthesis, *Global and Planetary Change*, 77, 85 – 96, <https://doi.org/https://doi.org/10.1016/j.gloplacha.2011.03.004>, 2011.

- Shupe, M. D.: A ground-based multisensor cloud phase classifier, *Geophysical Research Letters - GEOPHYS RES LETT*, 34, <https://doi.org/10.1029/2007GL031008>, 2007.
- Shupe, M. D.: ShupeTurner cloud microphysics, <https://doi.org/10.5439/1871015>, 2022.
- Shupe, M. D. and Intrieri, J. M.: Cloud Radiative Forcing of the Arctic Surface: The Influence of Cloud Properties, Surface Albedo, and Solar Zenith Angle, *Journal of Climate*, 17, 616–628, [https://doi.org/10.1175/1520-0442\(2004\)017<0616:CRFOTA>2.0.CO;2](https://doi.org/10.1175/1520-0442(2004)017<0616:CRFOTA>2.0.CO;2), 2004.
- Shupe, M. D. and Rex, M.: A Year in the Changing Arctic Sea Ice, *Oceanography*, <https://doi.org/10.5670/oceanog.2022.126>, 2022.
- Shupe, M. D., Uttal, T., and Matrosov, S. Y.: Arctic Cloud Microphysics Retrievals from Surface-Based Remote Sensors at SHEBA, *Journal of Applied Meteorology*, 44, 1544–1562, <https://doi.org/10.1175/JAM2297.1>, 2005.
- Shupe, M. D., Walden, V. P., Eloranta, E., Uttal, T., Campbell, J. R., Starkweather, S. M., and Shiobara, M.: Clouds at Arctic Atmospheric Observatories. Part I: Occurrence and Macrophysical Properties, *Journal of Applied Meteorology and Climatology*, 50, 626–644, <https://doi.org/10.1175/2010JAMC2467.1>, 2011.
- Shupe, M. D., Turner, D. D., Zwink, A., Thieman, M. M., Mlawer, E. J., and Shippert, T.: Deriving Arctic Cloud Microphysics at Barrow, Alaska: Algorithms, Results, and Radiative Closure, *Journal of Applied Meteorology and Climatology*, 54, 1675–1689, <https://doi.org/10.1175/JAMC-D-15-0054.1>, 2015.
- Shupe, M. D., Rex, M., Dethloff, K., Damm, E., Fong, A. A., Gradinger, R., Heuzé, C., Loose, B., Makarov, A., Maslowski, W., Nicolaus, M., Perovich, D., Rabe, B., Rinke, A., Sokolov, V., and Sommerfeld, A.: Arctic report card 2020: The MOSAiC expedition: A year drifting with the arctic sea ice, 2020.
- Shupe, M. D., Rex, M., Blomquist, B., Persson, P. O. G., Schmale, J., Uttal, T., Althausen, D., Angot, H., Archer, S., Bariteau, L., Beck, I., Bilberry, J., Bucci, S., Buck, C., Boyer, M., Brasseur, Z., Brooks, I. M., Calmer, R., Cassano, J., Castro, V., Chu, D., Costa, D., Cox, C. J., Creamean, J., Crewell, S., Dahlke, S., Damm, E., de Boer, G., Deckelmann, H., Dethloff, K., Dütsch, M., Ebell, K., Ehrlich, A., Ellis, J., Engelmann, R., Fong, A. A., Frey, M. M., Gallagher, M. R., Ganzeveld, L., Gradinger, R., Graeser, J., Greenamyre, V., Griesche, H., Griffiths, S., Hamilton, J., Heinemann, G., Helmig, D., Herber, A., Heuzé, C., Hofer, J., Houchens, T., Howard, D., Inoue, J., Jacobi, H.-W., Jaiser, R., Jokinen, T., Jourdan, O., Jozef, G., King, W., Kirchaessner, A., Klingebiel, M., Krassovski, M., Krumpfen, T., Lampert, A., Landing, W., Laurila, T., Lawrence, D., Lonardi, M., Loose, B., Lüpkes, C., Maahn, M., Macke, A., Maslowski, W., Marsay, C., Maturilli, M., Mech, M., Morris, S., Moser, M., Nicolaus, M., Ortega, P., Osborn, J., Pätzold, F., Perovich, D. K., Petäjä, T., Pilz, C., Pirazzini, R., Posman, K., Powers, H., Pratt, K. A., Preußner, A., Quéléver, L., Radenz, M., Rabe, B., Rinke, A., Sachs, T., Schulz, A., Siebert, H., Silva, T., Solomon, A., Sommerfeld, A., Spreen, G., Stephens, M., Stohl, A., Svensson, G., Uin, J., Viegas, J., Voigt, C., von der Gathen, P., Wehner, B., Welker, J. M., Wendisch, M., Werner, M., Xie, Z., and Yue, F.: Overview of the MOSAiC expedition: Atmosphere, *Elementa: Science of the Anthropocene*, 10, 00 060, <https://doi.org/10.1525/elementa.2021.00060>, 2022.
- Sivaraman, C., Flynn, D., Riihimäki, L., Comstock, J., and Zhang, D.: Cloud Mask from Micropulse Lidar, <https://doi.org/10.5439/1508389>, 2019.
- Sledd, A. and L'Ecuyer, T.: How Much Do Clouds Mask the Impacts of Arctic Sea Ice and Snow Cover Variations? Different Perspectives from Observations and Reanalyses, *Atmosphere*, 10, <https://doi.org/10.3390/atmos10010012>, 2019.
- Solomon, A., Shupe, M. D., Svensson, G., Barton, N. P., Batrak, Y., Bazile, E., Day, J. J., Doyle, J. D., Frank, H. P., Keeley, S., Remes, T., and Tolstykh, M.: The winter central Arctic surface energy budget: A model evaluation using observations from the MOSAiC campaign, *Elementa: Science of the Anthropocene*, 11, 00 104, <https://doi.org/10.1525/elementa.2022.00104>, 2023.

- Stapf, J., Ehrlich, A., Jäkel, E., Lüpkes, C., and Wendisch, M.: Reassessment of shortwave surface cloud radiative forcing in the Arctic: consideration of surface-albedo–cloud interactions, *Atmospheric Chemistry and Physics*, 20, 9895–9914, <https://doi.org/10.5194/acp-20-9895-2020>, 2020.
- Stubenrauch, C. J., Rossow, W. B., Kinne, S., Ackerman, S., Cesana, G., Chepfer, H., Girolamo, L. D., Getzewich, B., Guignard, A., Heidinger, A., Maddux, B. C., Menzel, W. P., Minnis, P., Pearl, C., Platnick, S., Poulsen, C., Riedi, J., Sun-Mack, S., Walther, A., Winker, D., Zeng, S., and Zhao, G.: Assessment of Global Cloud Datasets from Satellites: Project and Database Initiated by the GEWEX Radiation Panel, *Bulletin of the American Meteorological Society*, 94, 1031 – 1049, <https://doi.org/10.1175/BAMS-D-12-00117.1>, 2013.
- Svensson, G., Murto, S., Shupe, M. D., Pithan, F., Magnusson, L., Day, J. J., Doyle, J. D., Renfrew, I. A., Spengler, T., and Vihma, T.: Warm air intrusions reaching the MOSAiC expedition in April 2020—The YOPP targeted observing period (TOP), *Elementa: Science of the Anthropocene*, 11, 00 016, <https://doi.org/10.1525/elementa.2023.00016>, 2023.
- Tan, I. and Storelvmo, T.: Evidence of Strong Contributions From Mixed-Phase Clouds to Arctic Climate Change, *Geophysical Research Letters*, 46, 2894–2902, <https://doi.org/10.1029/2018GL081871>, 2019.
- Taylor, P. C., Boeke, R. C., Boisvert, L. N., Feldl, N., Henry, M., Huang, Y., Langen, P. L., Liu, W., Pithan, F., Sejas, S. A., and Tan, I.: Process Drivers, Inter-Model Spread, and the Path Forward: A Review of Amplified Arctic Warming, *Frontiers in Earth Science*, 9, <https://doi.org/10.3389/feart.2021.758361>, 2022.
- Taylor, P. C., Langen, P. L., and Tan, I.: Editorial: Arctic amplification: Feedback process interactions and contributions, *Frontiers in Earth Science*, 11, <https://doi.org/10.3389/feart.2023.1140871>, 2023.
- Uttal, T., Starkweather, S., Drummond, J. R., Vihma, T., Makshtas, A. P., Darby, L. S., Burkhart, J. F., Cox, C. J., Schmeisser, L. N., Haiden, T., Maturilli, M., Shupe, M. D., Boer, G. D., Saha, A., Grachev, A. A., Crepinsek, S. M., Bruhwiler, L., Goodison, B., McArthur, B., Walden, V. P., Dlugokencky, E. J., Persson, P. O. G., Lesins, G., Laurila, T., Ogren, J. A., Stone, R., Long, C. N., Sharma, S., Massling, A., Turner, D. D., Stanitski, D. M., Asmi, E., Aurela, M., Skov, H., Eleftheriadis, K., Virkkula, A., Platt, A., Förlund, E. J., Iijima, Y., Nielsen, I. E., Bergin, M. H., Candlish, L., Zimov, N. S., Zimov, S. A., O’Neill, N. T., Fogal, P. F., Kivi, R., Konopleva-Akish, E. A., Verlinde, J., Kustov, V. Y., Vassel, B., Ivakhov, V. M., Viisanen, Y., and Intrieri, J. M.: International Arctic Systems for Observing the Atmosphere: An International Polar Year Legacy Consortium, *Bulletin of the American Meteorological Society*, 97, 1033 – 1056, <https://doi.org/10.1175/BAMS-D-14-00145.1>, 2016.
- Walbröl, A., Crewell, S., Engelmann, R., Orlandi, E., Griesche, H., Radenz, M., Hofer, J., Althausen, D., Maturilli, M., and Ebell, K.: Atmospheric temperature, water vapour and liquid water path from two microwave radiometers during MOSAiC, *Scientific Data*, 9, 534, <https://doi.org/10.1038/s41597-022-01504-1>, 2022.
- Wang, M., Johnson, K., and Giangrande, S.: [arsclwacr1kolliasshp.c0](https://doi.org/10.5439/1823070), <https://doi.org/10.5439/1823070>, 2022.
- Webster, M. A., Holland, M., Wright, N. C., Hendricks, S., Hutter, N., Itkin, P., Light, B., Linhardt, F., Perovich, D. K., Raphael, I. A., Smith, M. M., von Albedyll, L., and Zhang, J.: Spatiotemporal evolution of melt ponds on Arctic sea ice: MOSAiC observations and model results, *Elementa: Science of the Anthropocene*, 10, 000 072, <https://doi.org/10.1525/elementa.2021.000072>, 2022.
- Wendisch, M., Macke, A., Ehrlich, A., Lüpkes, C., Mech, M., Chechin, D., Dethloff, K., Velasco, C. B., Bozem, H., Brückner, M., Clemen, H.-C., Crewell, S., Donth, T., Dupuy, R., Ebell, K., Egerer, U., Engelmann, R., Engler, C., Eppers, O., Gehrman, M., Gong, X., Gottschalk, M., Gourbeyre, C., Griesche, H., Hartmann, J., Hartmann, M., Heinold, B., Herber, A., Herrmann, H., Heygster, G., Hoor, P., Jafariserajehlou, S., Jäkel, E., Järvinen, E., Jourdan, O., Kästner, U., Kecorius, S., Knudsen, E. M., Köllner, F., Kretzschmar, J., Lelli, L., Leroy, D., Maturilli, M., Mei, L., Mertes, S., Mioche, G., Neuber, R., Nicolaus, M., Nomokonova, T., Notholt, J., Palm, M., van Pinxteren, M., Quaas, J., Richter, P., Ruiz-Donoso, E., Schäfer, M., Schmieder, K., Schnaiter, M., Schneider, J., Schwarzenböck, A., Seifert, P.,

- Shupe, M. D., Siebert, H., Spreen, G., Stapf, J., Stratmann, F., Vogl, T., Welti, A., Wex, H., Wiedensohler, A., Zanatta, M., and Zeppenfeld, S.: The Arctic Cloud Puzzle: Using ALOUD/PASCAL Multiplatform Observations to Unravel the Role of Clouds and Aerosol Particles in Arctic Amplification, *Bulletin of the American Meteorological Society*, 100, 841–871, <https://doi.org/10.1175/BAMS-D-18-0072.1>, 2019.
- Wendisch, M., Brückner, M., Crewell, S., Ehrlich, A., Notholt, J., Lüpkes, C., Macke, A., Burrows, J. P., Rinke, A., Quaas, J., Maturilli, M., Schemann, V., Shupe, M. D., Akansu, E. F., Barrientos-Velasco, C., Bärfuss, K., Blechschmidt, A.-M., Block, K., Bougoudis, I., Bozem, H., Böckmann, C., Bracher, A., Bresson, H., Bretschneider, L., Buschmann, M., Chechin, D. G., Chylik, J., Dahlke, S., Deneke, H., Dethloff, K., Donth, T., Dorn, W., Dupuy, R., Ebell, K., Egerer, U., Engelmann, R., Eppers, O., Gerdes, R., Gierens, R., Gorodetskaya, I. V., Gottschalk, M., Griesche, H., Gryanik, V. M., Handorf, D., Harm-Altstädter, B., Hartmann, J., Hartmann, M., Heinold, B., Herber, A., Herrmann, H., Heygster, G., Höschel, I., Hofmann, Z., Hölemann, J., Hünerbein, A., Jafariserajehlou, S., Jäkel, E., Jacobi, C., Janout, M., Jansen, F., Jourdan, O., Jurányi, Z., Kalesse-Los, H., Kanzow, T., Käthner, R., Kliesch, L. L., Klingebiel, M., Knudsen, E. M., Kovács, T., Körtke, W., Krampe, D., Kretzschmar, J., Kreyling, D., Kulla, B., Kunkel, D., Lampert, A., Lauer, M., Lelli, L., von Lerber, A., Linke, O., Löhnert, U., Lonardi, M., Losa, S. N., Losch, M., Maahn, M., Mech, M., Mei, L., Mertes, S., Metzner, E., Mewes, D., Michaelis, J., Mioche, G., Moser, M., Nakoudi, K., Neggers, R., Neuber, R., Nomokonova, T., Oelker, J., Papakonstantinou-Presvelou, I., Pätzold, F., Pefanis, V., Pohl, C., van Pinxteren, M., Radovan, A., Rhein, M., Rex, M., Richter, A., Risse, N., Ritter, C., Rostosky, P., Rozanov, V. V., Donoso, E. R., Garfias, P. S., Salzmann, M., Schacht, J., Schäfer, M., Schneider, J., Schnierstein, N., Seifert, P., Seo, S., Siebert, H., Soppa, M. A., Spreen, G., Stachlewska, I. S., Stapf, J., Stratmann, F., Tegen, I., Viceto, C., Voigt, C., Vountas, M., Walbröl, A., Walter, M., Wehner, B., Wex, H., Willmes, S., Zanatta, M., and Zeppenfeld, S.: Atmospheric and Surface Processes, and Feedback Mechanisms Determining Arctic Amplification: A Review of First Results and Prospects of the (AC)3 Project, *Bulletin of the American Meteorological Society*, 104, E208 – E242, <https://doi.org/10.1175/BAMS-D-21-0218.1>, 2023.
- Wilber, A., Kratz, D., and Gupta, S.: Surface Emissivity Maps for Use in Retrievals of Longwave Radiation Satellite, [https://www-calipso.larc.nasa.gov/resources/calipso\\_users\\_guide/data\\_summaries/pdfs/Wilber.NASATchNote99.pdf](https://www-calipso.larc.nasa.gov/resources/calipso_users_guide/data_summaries/pdfs/Wilber.NASATchNote99.pdf), last access: 01/11/2024, 1999.
- Witthuhn, J., Hünerbein, A., Filipitsch, F., Wacker, S., Meilinger, S., and Deneke, H.: Aerosol properties and aerosol–radiation interactions in clear sky conditions over Germany, *Atmospheric Chemistry and Physics Discussions*, 2021, 1–64, <https://doi.org/10.5194/acp-2021-517>, 2021.
- Węglarczyk, Stanisław: Kernel density estimation and its application, *ITM Web Conf.*, 23, 00037, <https://doi.org/10.1051/itmconf/20182300037>, 2018.
- Zhang, D.: mwrret1liljclou, <https://doi.org/10.5439/1027369>, 1996.
- Zib, B. J., Dong, X., Xi, B., and Kennedy, A.: Evaluation and Intercomparison of Cloud Fraction and Radiative Fluxes in Recent Reanalyses over the Arctic Using BSRN Surface Observations, *Journal of Climate*, 25, 2291–2305, <https://doi.org/10.1175/JCLI-D-11-00147.1>, 2012.

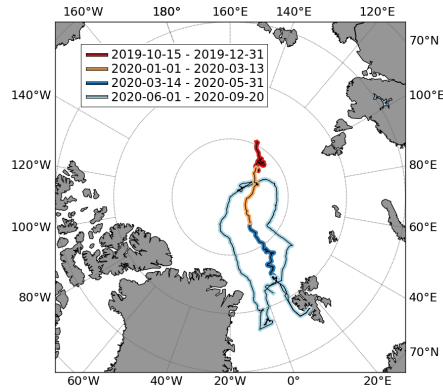


**Figure 1.** The cruise track of the research vessel Polarstern during the MOSAiC expedition is shown on an Arctic polar stereographic map. The red and orange solid lines show the track during the polar night, and the blue and light blue solid lines denote the track during the polar day. Each colour represents the period shown in the upper box discussed in Section 4.2.

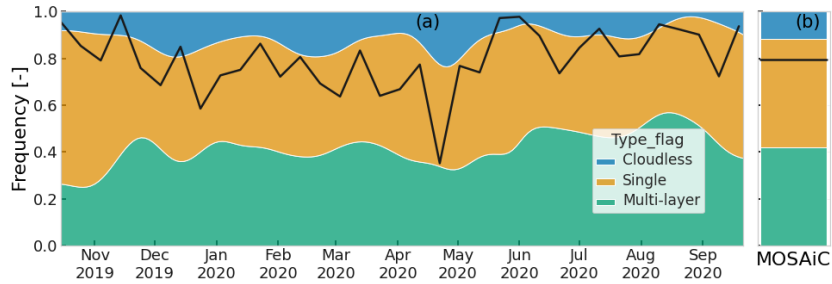


**Figure 2.** Time series showing the occurrence and composition of clouds during MOSAiC. Panel a shows the occurrence frequency of cloudless conditions (blue), single-layer clouds (orange), and multi-layer clouds (green), while the black line shows the cloud fraction from CERES SYN. The black line in panel a shows the 10-day averaged normalised cloud area fraction from CERES SYN, and mean values are shown in the black solid line in panel b.

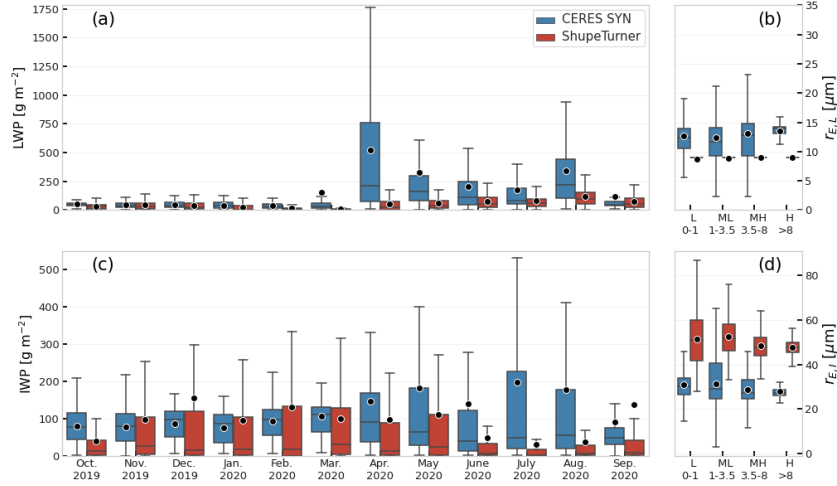


**Figure 3.** Time series of cloud water paths based on the ShupeTurner and CERES SYN retrievals. Panels a and c show box plots of monthly statistics of the liquid water path (LWP) and ice water path (IWP), respectively for the CERES SYN (blue) and ShupeTurner (red) datasets. Panels b and d show statistics of the vertical profiles of liquid droplet ( $r_{E,L}$ ) and ice crystals ( $r_{E,I}$ ) effective radius for low-level (L; 0-1 km), mid-low level (ML; 1-3.5 km), mid-high level (MH; 3.5-8 km), and high-level clouds (H; >8 km) for the entire MOSAiC expedition. Boxes in panels c-f extend from the 25th to 75th percentile, the median is represented by a line, and the black dots depict the mean.

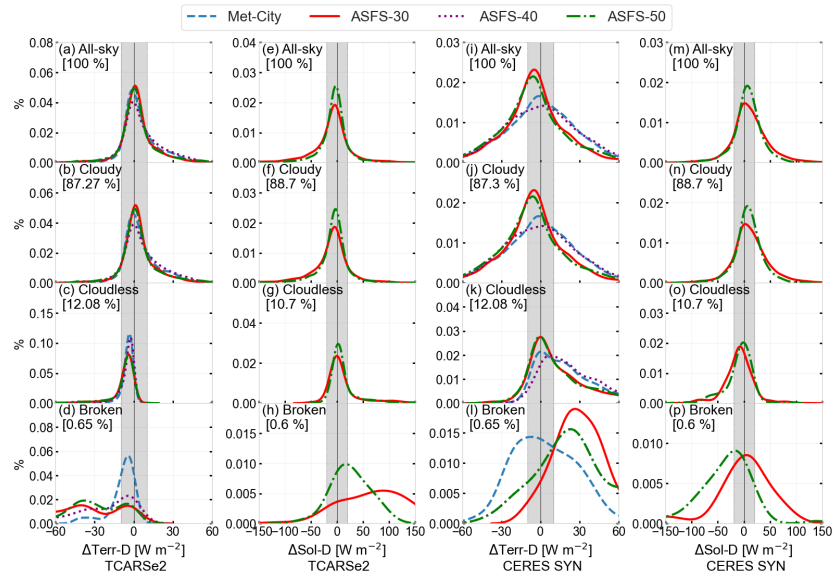


**Figure 4.** Kernel density estimate (KDE) of the distribution of differences between simulated and observed radiative fluxes at the surface. The first two columns show the KDE for the TCARS simulations, while the last two columns show the KDE for CERES SYN collocated to the positions of Met-City, ASFS-30, ASFS-40, and ASFS-50.

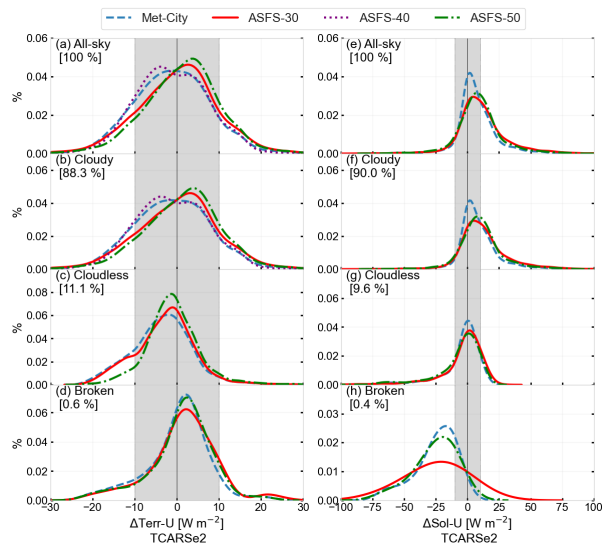
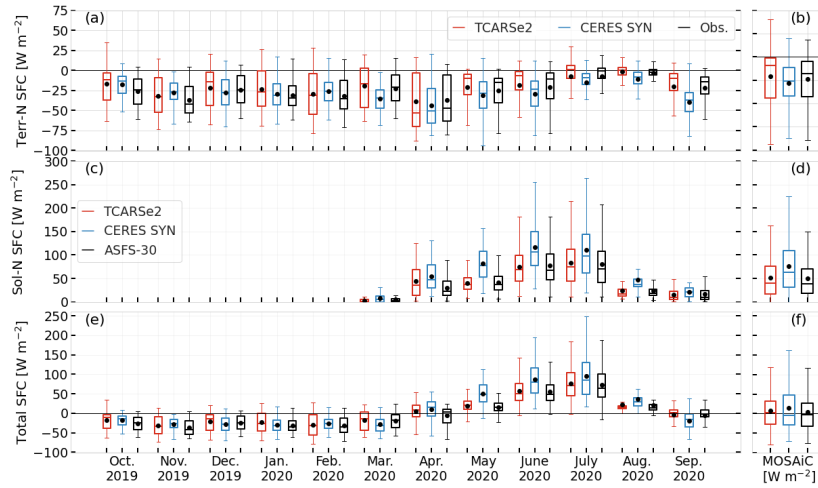


**Figure 5.** Same as Figure 4, but comparing the KDE of the difference between TCARS and CERES SYN fluxes at the TOA. **TCARSe1** simulations are considered for the Terra-U and TCARSe2 for the Sol-U comparison.



Time series of terrestrial (panels a, b) and solar flux (panels c, d) at the surface for TCARS simulations, CERES SYN product, and observations at the ASFS-30 station and Met-City for the last 15 days of October 2019. Panels e and f show the net radiation budget at the surface (SFC). Panels b, d and f show the mean values for the entire MOSAiC period. The box plot shows the distribution of the net fluxes.

Panel d shows the statistical values for the period when solar radiation is available during MOSAiC. The mean values for the entire MOSAiC expedition are indicated in Table 6.

Time series of terrestrial (panels a, b) and solar flux (panels c, d) at the surface for TCARS simulations, CERES SYN product, and observations at the ASFS-30 station and Met-City for the last 15 days of October 2019. Panels e and f show the net radiation budget at the surface (SFC). Panels b, d and f show the mean values for the entire MOSAiC period. The box plot shows the distribution of the net fluxes. Panel d shows the statistical values for the period when solar radiation is available during MOSAiC. The mean values for the entire MOSAiC expedition are indicated in Table 6.

**Figure 6.** Monthly distributions of net terrestrial flux (Terr-N) for TCARSe1 simulations, CERES SYN product and observations at the ASFS-30 station. For October and November 2019, an additional comparison is shown with observations at ASFS-40, and for March and April 2020, the Terr-N distributions at Met-City are included. Note that the distributions in November 2019 and September 2020 represent 15 and 20 days, respectively.

Time series of terrestrial (panels a, b) and solar flux (panels c, d) at the surface for TCARS simulations, CERES SYN product, and observations at the ASFS-30 station and Met-City for the last 15 days of October 2019. Panels e and f show the net radiation budget at the surface (SFC). Panels b, d and f show the mean values for the entire MOSAiC period. The box plot shows the distribution of the net fluxes. Panel d shows the statistical values for the period when solar radiation is available during MOSAiC. The mean values for the entire MOSAiC expedition are indicated in Table 6.

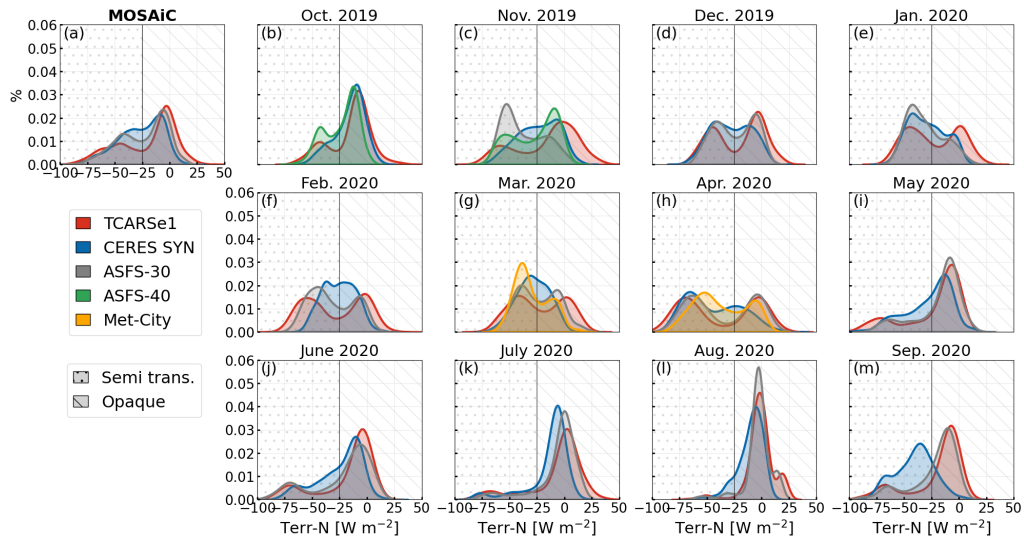


**Figure 7.** Monthly distributions of net terrestrial flux (Terr-N) at the surface for TCARSe1 simulations, CERES SYN product and observations at the ASFS-30 station. For October and November 2019, an additional comparison is shown with observations at ASFS-40, and for March and April 2020, the Terr-N distributions at Met-City are included. Note that the distributions in November 2019 and September 2020 represent 15 and 20 days, respectively.

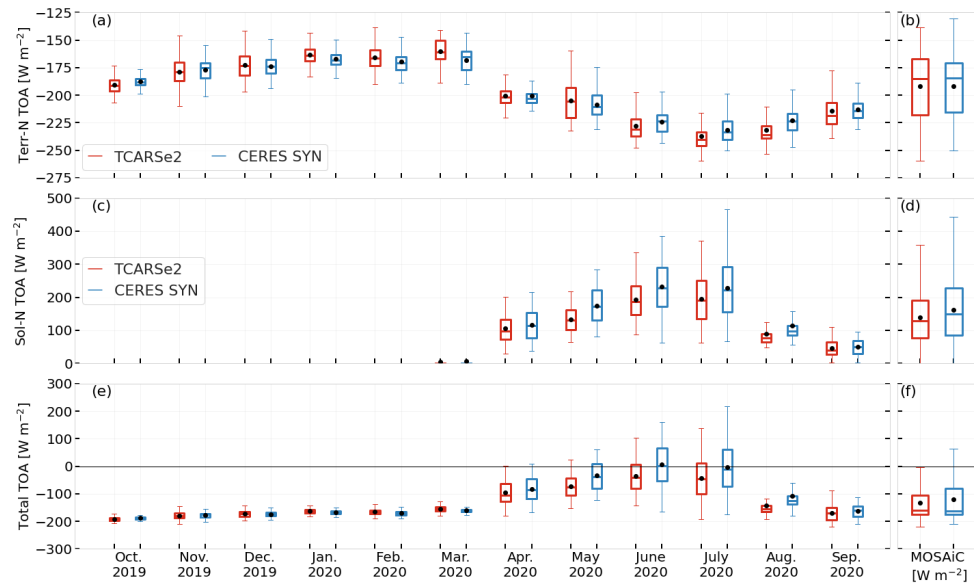


**Figure 8.** Time series shown as monthly box plots for the net terrestrial (Terr-N, panels a and b), net solar (Sol-N, panels c and d), and total flux at the top of the atmosphere (Net, panels e and f). The box plots for TCARS are displayed in red, while the ones for CERES SYN are shown in blue. Box plots for the entire MOSAiC period are displayed in panels b, d, and f. Panel d shows the statistical values for the period when solar radiation is available during MOSAiC. The mean values for the entire MOSAiC expedition are indicated in Table 6.

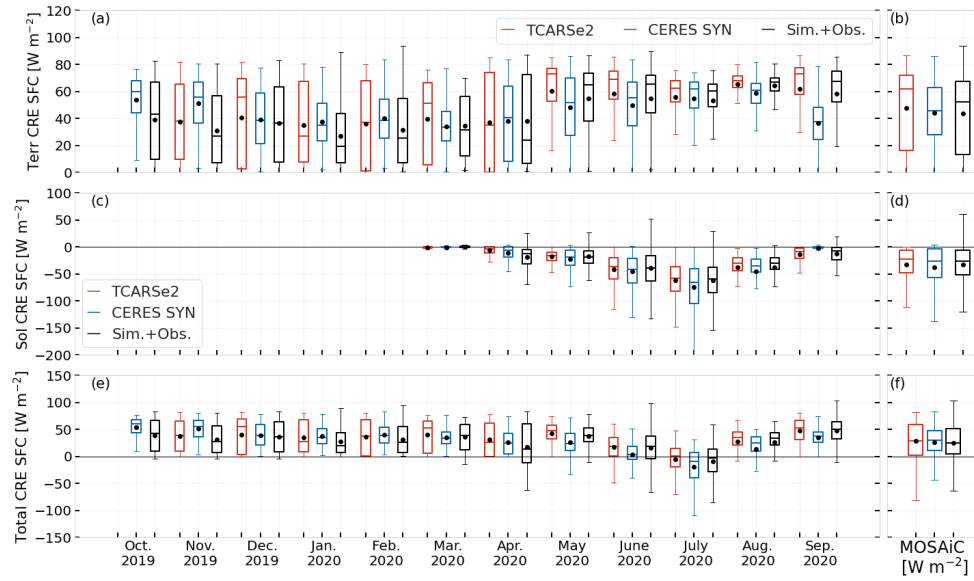


**Figure 9.** Time series of monthly box plots for the terrestrial (panel a), solar (panel b), and total (panel c) cloud radiative effect (CRE) at the surface. Box plots for the entire MOSAiC period are shown in panels b, d, and f. Panel d shows the statistical values for the period when solar radiation is available during MOSAiC. The mean values for the entire MOSAiC expedition are indicated in Table 6.

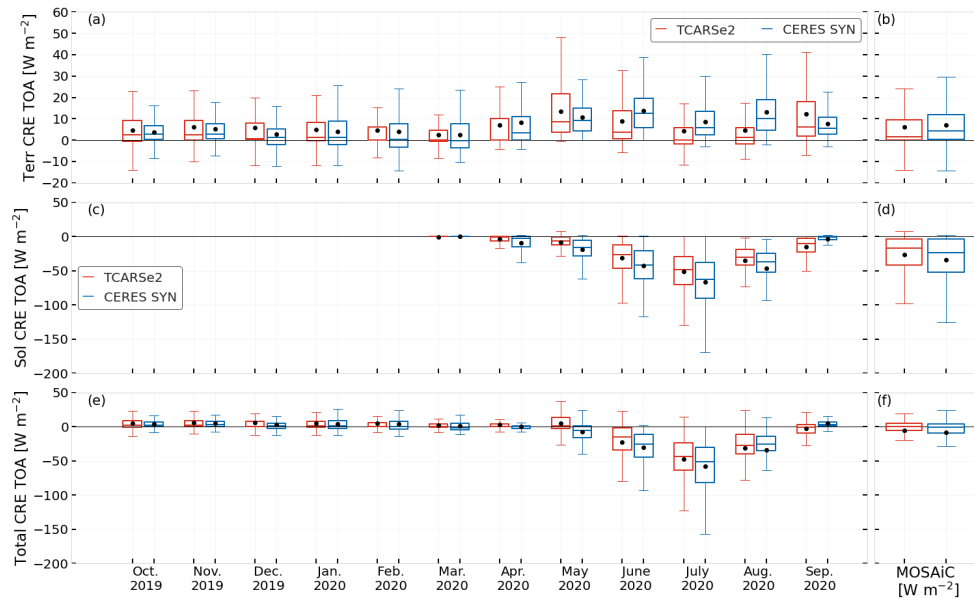


**Figure 10.** Time series of monthly box plots of the terrestrial (panel a), solar (panel b), and net (panel c) cloud radiative effect (CRE) at the TOA. Box plots for the entire MOSAiC period are shown in panels b, d, and f. Panel d shows the statistical values for the period when solar radiation is available during MOSAiC. The mean values for the entire MOSAiC expedition are indicated in Table 6.

**Table 1.** List of data sources for ShupeTurner retrievals as well as for the radiative transfer simulations (TCARS), and for supplementary analysis (SA).

|               | Instruments/Dataset                        | Measurements  | References   |
|---------------|--|---|--|
| 7*ShupeTurner | Micropulse lidar (MPL)                     | Backscatter and depolarization ratio  | Sivaraman et al. (2019)  |
|               | Ceilometer                                 | Cloud base  | Morris et al. (1996)   |
|               | 2*Ka-band ARM Zenith Radar (KAZR)          | Doppler radar, reflectivity, spectra<br>Best estimates of cloud boundaries  | Johnson et al. (2014)<br>Wang et al. (2022)  |
|               | Radiosondes                                | Interpolation of atmospheric properties   | Jensen et al. (1998)   |
|               | MiRAC-P radiometer                         | Liquid water path   | Ebell et al. (2022) Walbröl et al. (2022)  |
|               | ARM Microwave radiometer                   | Liquid water path   | Zhang (1996)   |
| 15*TCARS      | ShupeTurner                                | Cloud properties  | Shupe (2022)   |
|               | 2*ERA5                                     | Atmospheric pressure, temperature,<br>specific humidity, ozone, and surface pressure  | 2*Hersbach et al. (2020)   |
|               | NOAA Annual Greenhouse<br>Gas Index (AGGI) | CO mole fraction<br>CO <sub>2</sub> mole fraction<br>CH <sub>4</sub> mole fraction<br>N <sub>2</sub> O mole fraction<br>CCL <sub>4</sub> mole fraction<br>CFC-12 mole fraction<br>CFC-11 mole fraction<br>HCFC-22 mole fraction | NOAA-AGGI (2024)<br>Lan et al. (2022a)<br>Lan et al. (2022b)<br>Dutton et al. (2023a)<br>Dutton et al. (2023b)<br>Dutton et al. (2023c)<br>Dutton et al. (2023d)<br>Montzka (2024) |
|               | 2*ASFS-30                                  | Skin temperature<br>Daily mean surface albedo   | Cox et al. (2023b)<br>Cox et al. (2023b)   |
|               | ASFS-50                                    | Daily mean surface albedo   | Cox et al. (2023d)   |
|               | CERES SYN                                  | Surface albedo and ice fraction   | Rutan et al. (2015)  |
| 5*SA          | Met-City                                   | Skin temperature, radiative fluxes  | Cox et al. (2023a)   |
|               | ASFS-30                                    | Skin temperature, radiative fluxes  | Cox et al. (2023b)   |
|               | ASFS-40                                    | Skin temperature, radiative fluxes  | Cox et al. (2023c)   |
|               | ASFS-50                                    | Skin temperature, radiative fluxes  | Cox et al. (2023d)   |
|               | Radiosondes                                | Blend products of atmospheric properties  | Dahlke et al. (2023)   |

**Table 2.** Hourly downwelling terrestrial flux difference (FD) at the surface (SFC) for the entire MOSAiC period under different atmospheric conditions in  $W m^{-2}$ . Results are based on TCARS simulations, CERES SYN product (CERES), and observations at ASFS-30. An additional comparison for CERES SYN cloudless (CS) products is given for cloudless and broken cloud conditions.

| Atm. Cond.      |        | All-sky |       | Cloudy  |       | Cloudless |             | Broken  |             |
|-----------------|--------|---------|-------|---------|-------|-----------|-------------|---------|-------------|
| FD              |        | TCARSe1 | CERES | TCARSe1 | CERES | TCARSe1   | CERES (CS)  | TCARSe1 | CERES (CS)  |
| Terr-D<br>(SFC) | Mean   | 3.2     | -4.4  | 3.9     | -4.9  | -8.0      | 13.2 (-9.9) | -32.7   | 4.8 (-38.3) |
|                 | Median | 1.8     | -4.7  | 2.2     | -5.2  | -4.8      | 6.5 (-6.2)  | -36.5   | 1.6 (-42.0) |
|                 | RMSE   | 14.0    | 24.5  | 14.2    | 24.4  | 13.9      | 25.6 (17.3) | 40.7    | 25.9 (45.0) |
|                 | SD     | 13.6    | 24.1  | 13.6    | 23.9  | 11.3      | 21.9 (14.2) | 24.2    | 25.4 (21.2) |

**Table 3.** Hourly downwelling solar (Sol-D) flux difference (FD) at the surface (SFC) for the entire MOSAiC period under different atmospheric conditions in  $W m^{-2}$ . Results are shown for CERES SYN (CERES) products, TCARS simulations using different surface albedo based on CERES SYN surface albedo (TCARSe1), daily mean from observations at ASFS-30 (TCARSe2), and at ASFS50 (TCARSe3). An additional comparison for CERES SYN cloudless (CS) products is given for cloudless and broken cloud conditions.

| Atm. Cond.     |        | All-sky   |         |         |             | Cloudy  |         |         |             |
|----------------|--------|-----------|---------|---------|-------------|---------|---------|---------|-------------|
| FD             |        | TCARSe1   | TCARSe2 | TCARSe3 | CERES       | TCARSe1 | TCARSe2 | TCARSe3 | CERES       |
| Sol-D<br>(SFC) | Mean   | -11.8     | -1.7    | 3.9     | 12.3        | -13.4   | 4.0     | 4.8     | 13.0        |
|                | Median | -5.9      | -1.0    | 1.8     | 9.4         | -6.8    | 1.7     | 3.5     | 10.2        |
|                | RMSE   | 45.7      | 41.6    | 35.6    | 39.3        | 46.3    | 39.4    | 41.2    | 39.6        |
|                | SD     | 44.1      | 41.5    | 35.4    | 37.3        | 44.3    | 39.2    | 40.9    | 37.4        |
| Atm. Cond.     |        | Cloudless |         |         |             | Broken  |         |         |             |
| FD             |        | TCARSe1   | TCARSe2 | TCARSe3 | CERES (CS)  | TCARSe1 | TCARSe2 | TCARSe3 | CERES (CS)  |
| Sol-D<br>(SFC) | Mean   | 12.4      | 14.6    | 19.3    | -10.2 (7.3) | 75.4    | 82.3    | 77.0    | -3.0 (59.7) |
|                | Median | 1.3       | 3.3     | 5.0     | -8.3 (-0.5) | 76.9    | 83.8    | 78.8    | 7.6 (54.9)  |
|                | RMSE   | 37.7      | 39.3    | 42.9    | 33.2 (33.9) | 102.2   | 108.3   | 97.0    | 57.5 (91.0) |
|                | SD     | 35.6      | 36.5    | 38.3    | 31.6 (33.0) | 69.0    | 70.5    | 58.9    | 57.4 (61.7) |

**Table 4.** Hourly radiative flux difference (FD) at the top-of-the-atmosphere (TOA) for the entire MOSAiC period under different atmospheric conditions. Results are based on TCARS simulations and CERES SYN observations in  $W m^{-2}$ .

| Atm. Cond.      |        | All-sky | Cloudy  | Cloudless | Broken  |
|-----------------|--------|---------|---------|-----------|---------|
| FD              |        | TCARSe1 | TCARSe1 | TCARSe1   | TCARSe1 |
| Terr-U<br>(TOA) | Mean   | 0.3     | 0.4     | -2.8      | 1.5     |
|                 | Median | 0.7     | 0.9     | -2.3      | 2.0     |
|                 | RMSE   | 9.6     | 9.7     | 7.7       | 8.0     |
|                 | SD     | 9.6     | 9.7     | 7.1       | 7.9     |

**Table 5.** Hourly upwelling solar (Sol-U) flux difference (FD) at the top-of-the-atmosphere (TOA) for the entire MOSAiC period under different atmospheric conditions in  $W m^{-2}$ . Results are shown for CERES SYN (CERES) products, TCARS simulations using different surface albedo based on CERES SYN surface albedo (TCARSe1), daily mean from observations at ASFS-30 (TCARSe2), and at ASFS50 (TCARSe3). An additional comparison for CERES SYN cloudless (CS) products is given for cloudless and broken cloud conditions.

| Atm. Cond.     |        | All-sky       |         |         | Cloudy  |         |         |
|----------------|--------|---------------|---------|---------|---------|---------|---------|
| FD             |        | TCARSe1       | TCARSe2 | TCARSe3 | TCARSe1 | TCARSe2 | TCARSe3 |
| Sol-U<br>(TOA) | Mean   | 11.4          | 26.8    | 22.7    | 12.4    | 26.8    | 22.5    |
|                | Median | 8.9           | 20.8    | 17.4    | 9.6     | 21.0    | 17.5    |
|                | RMSE   | 23.7          | 38.4    | 35.2    | 23.9    | 38.2    | 34.7    |
|                | SD     | 20.8          | 27.5    | 26.9    | 20.4    | 27.2    | 26.4    |
| Atm. Cond.     |        | Cloudless sky |         |         | Broken  |         |         |
| FD             |        | TCARSe1       | TCARSe2 | TCARSe3 | TCARSe1 | TCARSe2 | TCARSe3 |
| Sol-U<br>(TOA) | Mean   | -4.0          | 21.0    | 17.0    | -35.6   | 36.3    | 30.6    |
|                | Median | 0.0           | 10.4    | 8.2     | -22.8   | 21.6    | 14.4    |
|                | RMSE   | 18.9          | 39.9    | 38.9    | 61.2    | 56.3    | 55.2    |
|                | SD     | 18.4          | 34.0    | 35.0    | 49.7    | 43.0    | 45.9    |

**Table 6.** Mean hourly values of the radiation budget during MOSAiC in  $W m^{-2}$ . Values in parentheses indicate the standard deviation (SD). The percentage is given for the temporal coverage of the available simulations for MOSAiC. The calculations of the observations (Obs.) are based mostly on ASFS-30 observations except for October 2019, when the observations at Met-City are considered due to temporal coverage. Two calculations are considered for CERES SYN, the first one for 100 % temporal coverage as in TCARSe1 and then for 97.2 % of the same temporal coverage as TCARSe2 simulations. *Note that the values for each flux was calculated for the entire MOSAiC period.*

| Data       |        | TCARSe1                | TCARSe2                | TCARSe3<br>CERES SYN       | CERES SYN              | Obs.                       |
|------------|--------|------------------------|------------------------|----------------------------|------------------------|----------------------------|
| Percentage |        | 100 %                  | 97.2 %                 | 76.5 %<br>100 %            | 97.2 %                 | 97.2 %                     |
| 4*TOA      | Terr-N | -193.6 (30.2)          | -192.0 (20.1)          | -188.2 (29.1)-193.7 (25.7) | -192.1 (25.9)          | -                          |
|            | Sol-N  | 71.3 (96.2)            | 59.7 (85.9)            | 41.8 (76.1)71.9 (102.5)    | 71.8 (103.2)           | -                          |
|            | Total  | -122.3 (77.1)          | -132.4 (65.7)          | -146.0 (57.5)-120.4 (83.0) | -120.4 (83.4)          | -                          |
|            | CRE    | -15.5 (40.0)           | -5.2 (24.8)            | -3.3 (23.2)-8.3 (27.5)     | -8.5 (27.6)            | -                          |
| 4*SFC      | Terr-N | -21.1 (26.7)           | -20.8 (26.5)           | -22.0 (26.7) -28.3 (20.6)  | -26.7 (19.9)           | -23.7 (22.7)               |
|            | Sol-N  | 64.0 (60.0)30.2 (51.9) | 50.2 (45.5)23.6 (40.6) | 50.4 (49.0)34.1 (53.7)     | 72.2 (57.9)34.9 (56.1) | 74.3 (58.0)46.9 (43.8)22.1 |
|            | Total  | 17.8 (58.7)            | 1.7 (44.9)9.9 (49.2)   | 1.1 (46.7) 15.6 (59.1)     | 15.9 (59.6)12.8 (58.3) | 3.9 (46.2)4.7 (46.1)       |
|            | CRE    | 19.5 (41.1)            | 29.3 (32.8)            | 30.6 (33.2) 22.8 (31.8)    | 26.4 (31.8)            | 25.0 (32.4)                |

## Appendix A: Temporal coverage of radiative transfer simulations

Figure A2 illustrates the methodology of the radiative transfer simulations using TCARS framework (Fig. A1) and the temporal coverage of the different radiative transfer experiments created with TCARS (Fig. A2).

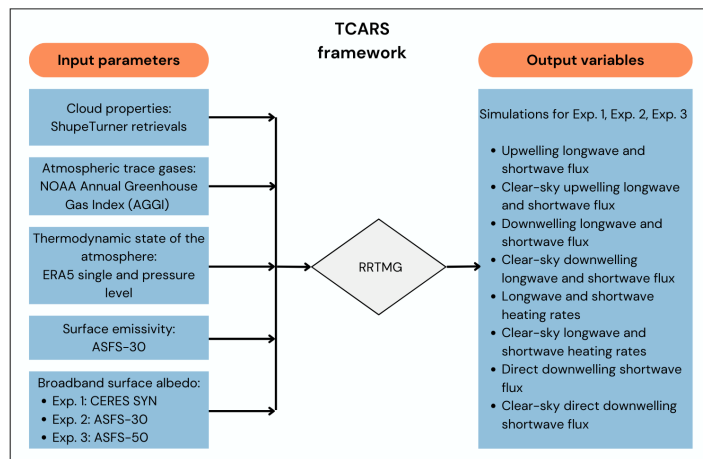


**Figure A1.** Flow chart showing the steps followed to obtain the radiative transfer simulations using the TCARS framework. The naming of output variables is given according to the dataset variable naming in (Barrientos-Velasco, 2024), referring to the solar fluxes as shortwave, and to the thermal fluxes as longwave.

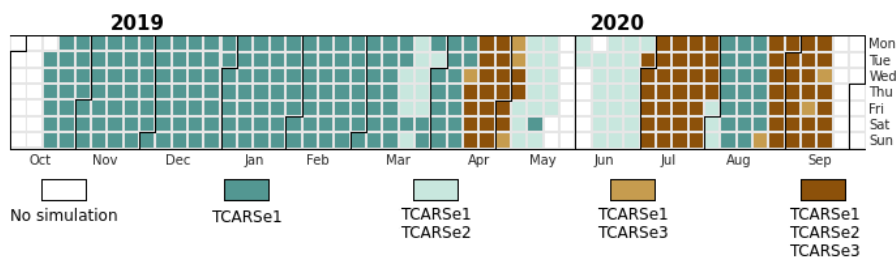


**Figure A2.** Calendar Heat map plot showing the temporal coverage of each experimental set of TCARS simulations for the MOSAiC period from 2019-10-15 to 2020-09-20.

## Appendix B: Atmospheric and Surface conditions

The atmospheric temperature during MOSAiC is illustrated in Fig. B1 based on ERA5 atmospheric profiles and the blended product from Dahlke et al. (2023) to illustrate the variation of this parameter in K.

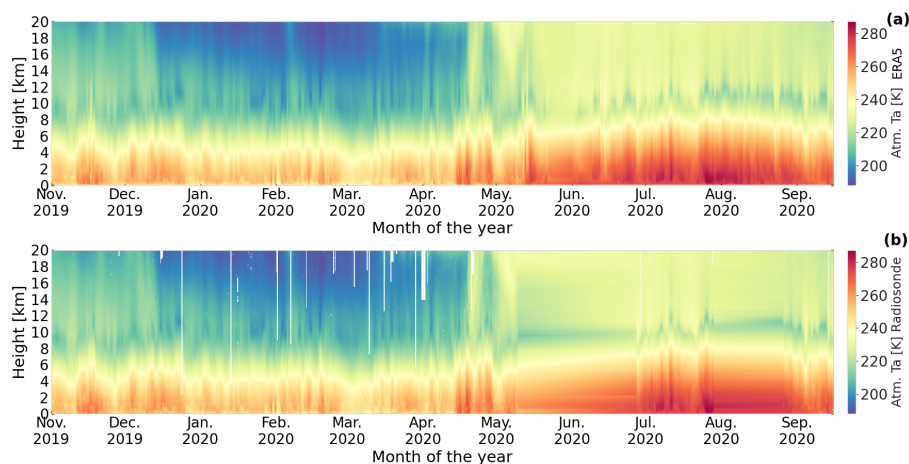


**Figure B1.** Time series of linearly interpolated atmospheric temperature for MOSAiC based on ERA5 (panel a), and merged radiosondes (panel b).

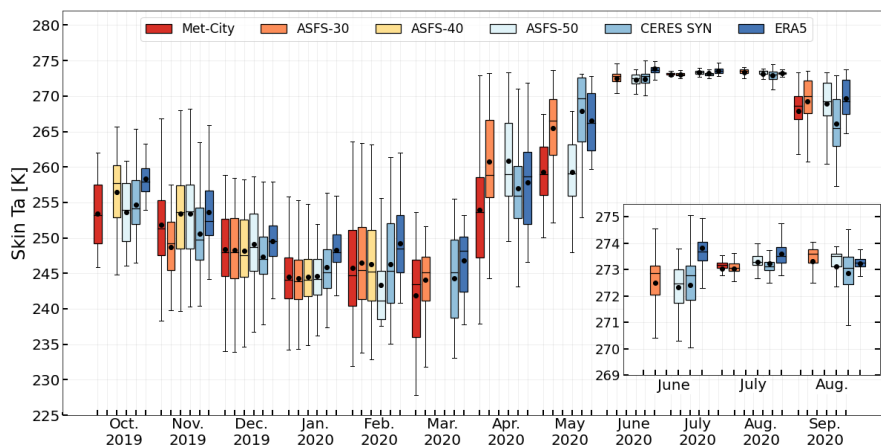


**Figure B2.** Monthly time series of box plots showing the distribution of skin temperature for MOSAiC based on ERA5, CERES SYN, and ice floe stations.

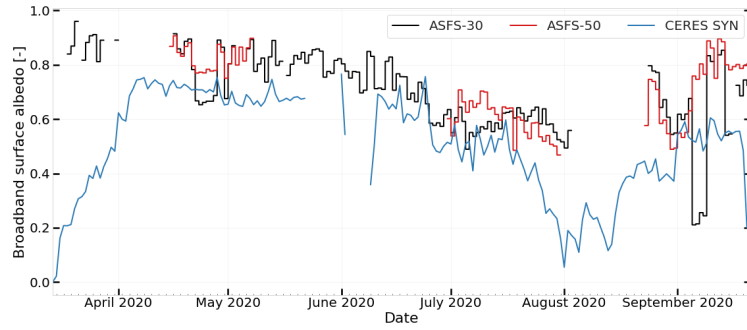


**Figure B3.** Time series of the daily mean broadband surface albedo from 2020-03-14 to 2020-09-20. Data gaps in the CERES SYN time series are subject to the overall data availability for the radiative transfer simulations.

### Appendix C: Comparison of cloudless simulations

Same as Fig. ??, but for the TOA.

Similar to panels c, d, g, and h, but for the TOA in Fig. C1.

Comparison of downwelling terrestrial radiative flux (Terr-D) at the surface for cloudless simulations between TCARS and CERES SYN: The first row shows the kernel density distribution of TCARS minus CERES SYN fluxes. The second row shows scatter plots comparing CERES SYN (y-axis) and TCARS simulations (x-axis). Linear regressions are shown by the red line. Mean, RMSE and correlation coefficient are indicated in each box. Each column depicts the results for each period indicated in the top panel.

Same as Fig. ??, but for the upwelling terrestrial flux (Terr-U) at the surface.

In all the plots of this section, the first row indicates the distribution of the Kernel Density Estimate (KDE) of the flux difference between TCARSe1 simulations minus CERES SYN product, and the second row presents the linear regression of each comparison. The KDE is a technique utilised to estimate the probability density function (PDF) from a collection of data points, producing a smooth estimate of the PDF. The shape of the KDE indicates the concentration of data points within the sample dataset (Węglarczyk, Stanisław, 2018).

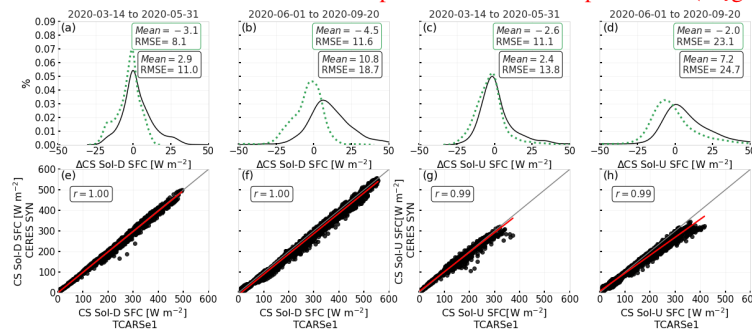


**Figure C1.** Comparison of downwelling solar radiative flux (Sol-D; panel a,b,e, and f) and upwelling solar radiative flux (Sol-U; panel c, d, g, and h) at the surface for cloudless simulations between TCARS and CERES SYN: The first row shows the kernel density estimate (KDE) distribution of TCARS minus CERES SYN fluxes. The second row shows scatter plots comparing CERES SYN (y-axis) and TCARS simulations (x-axis). Linear regressions are shown by the red line. Mean, RMSE and correlation coefficient are indicated in each box. Each column depicts the results for each period indicated in the top panel. The green dotted KDE distribution shown in panels a-d show the same comparison for CERES SYN fluxes for pristine conditions.

## Appendix D: Radiative flux difference for all available ice floe stations during MOSAiC

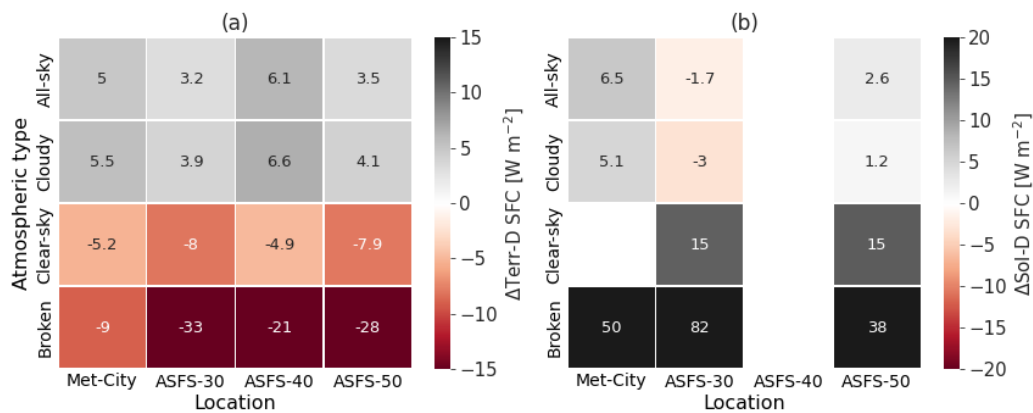


**Figure D1.** Mean flux difference between TCARSe1 simulations and observed broadband radiative fluxes for MOSAiC at the surface (SFC). Panel (a) and (b) show downwelling Terrestrial (Terr-D) and Solar (Sol-D) fluxes, respectively for all stations.

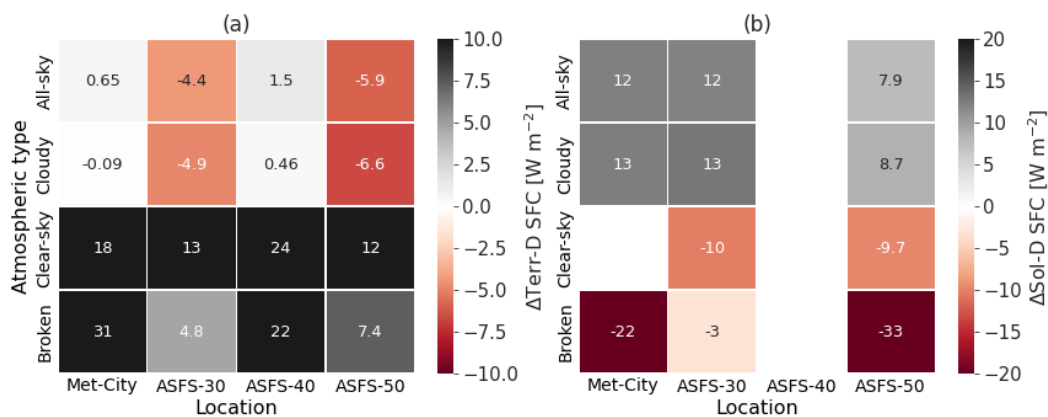


**Figure D2.** Same as Fig. D1 but comparing CERES SYN minus observations.

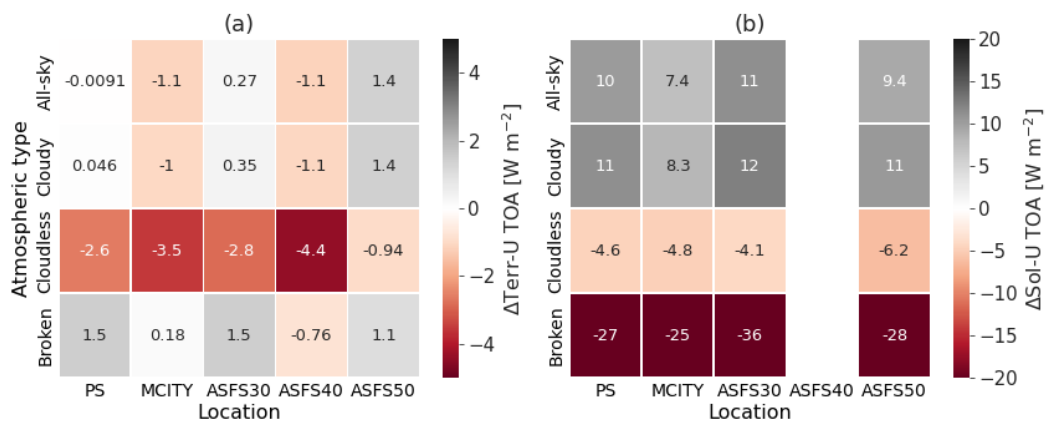


**Figure D3.** Mean flux difference between TCARS and CERES SYN fluxes at the TOA. Panel (a) shows biases for the upwelling terrestrial flux (Terr-U) considering TCARSe1, and (b) shows the comparison for the upwelling solar flux (Sol-U) using TCARSe2.

**Table A1.** List of Acronyms

| Abbreviation | Meaning  |
|--------------|--|
| AGGI         | Annual Greenhouse Gas Index  |
| Atm.         | Atmospheric  |
| ASFS         | Atmospheric Surface Flux Stations                                      |
| CERES        | Clouds and the Earth's Radiant Energy System                           |
| CERES SYN    | Clouds and the Earth's Radiant Energy System SYN Ed.4.1 product        |
| Cond.        | Conditions   |
| CS           | Cloudless  |
| CRE          | Cloud Radiative Effect   |
| Eff.         | Effective  |
| FD           | Flux difference  |
| KDE          | Kernel Density Estimate  |
| LWC          | Liquid water content   |
| LWP          | Liquid water path  |
| MOSAIc       | Multidisciplinary drifting Observatory for the Study of Arctic Climate |
| Net CRE      | Net cloud radiative effect (Terrestrial plus solar CRE)                |
| IWC          | Ice water content  |
| IWP          | Ice water path   |
| Obs.         | Observations   |
| PS           | <i>Polarstern</i>  |
| $r_{E,L}$    | Liquid droplet effective radius  |
| $r_{E,I}$    | Ice crystal effective radius   |
| RMSE         | Root mean squared error  |
| RRTMG        | Rapid radiative transfer model (RRTM) for GCM applications             |
| SFC          | Surface  |
| SO           | Surface Observatory  |
| Sol-D        | Broadband downwelling solar (shortwave) flux                           |
| Sol-N        | Broadband net solar (shortwave) flux                                   |
| Sol-U        | Broadband upwelling solar (shortwave) flux                             |
| SD           | Standard Deviation   |
| TCARS        | TROPOS Cloud and Aerosol Radiative effect Simulator                    |
| Terr-D       | Broadband downwelling terrestrial (longwave) flux                      |
| Terr-N       | Broadband net terrestrial (longwave) flux                              |
| Terr-U       | Broadband upwelling terrestrial (longwave) flux                        |
| TOA          | Top of the atmosphere  |
| Total flux   | Terr-N plus Sol-N  |

**Table A2.** Hourly radiative flux difference (FD) between simulated (TCARSe1) and observed downwelling fluxes at surface (SFC) and upwelling fluxes at the top-of-the-atmosphere (TOA) for single-layer clouds subdivided by cloud phase for the entire MOSAiC period in  $W m^{-2}$ . The flux comparison at the surface considers observations at the ASFS-30 station and the TOA products from CERES SYN. In parenthesis is given the frequency of occurrence of the different single-layer cloud types. Precipitating events accounted for 20 % of the time.

| Atm. Cond.      |        | Liquid (32.2 %) | Ice (33.1 %) | Mixed (14.7 %) |
|-----------------|--------|-----------------|--------------|----------------|
| FD              |        | TCARSe1         | TCARSe1      | TCARSe1        |
| Terr-U<br>(TOA) | Mean   | 7.4             | -2.8         | 0.6            |
|                 | Median | 6.4             | -3.0         | 2.1            |
|                 | RMSE   | 11.0            | 8.9          | 10.8           |
|                 | SD     | 8.2             | 8.4          | 10.8           |
| Terr-D<br>(SFC) | Mean   | 3.8             | -1.4         | 7.3            |
|                 | Median | 2.7             | -2.4         | 4.0            |
|                 | RMSE   | 16.0            | 21.6         | 16.2           |
|                 | SD     | 15.6            | 21.5         | 14.4           |

**Table A3.** The hourly radiative flux difference (FD) between TCARS and observations is measured in  $W m^{-2}$ . At the surface (SFC), downwelling fluxes are compared, while at the top-of-the-atmosphere (TOA), solar upwelling fluxes are analysed. These comparisons are conducted for single-layer clouds, which are further subdivided by cloud phase, over the entire MOSAiC period. Surface observations are obtained from the ASFS-30 station, and TOA observations are sourced from CERES SYN data. TCARS simulations using different surface albedo based on CERES SYN surface albedo (e1), daily mean from observations at ASFS-30 (e2), and at ASFS50 (e3). In parenthesis is given the frequency of occurrence of the different single-layer cloud types. Precipitating events accounted for 22.7 % of the time.

| Atm. Cond.     |        | Liquid (22.0 %) |      |      | Ice (16.8 %) |      |      | Mixed (38.5 %) |      |      |
|----------------|--------|-----------------|------|------|--------------|------|------|----------------|------|------|
| FD             |        | e1              | e2   | e3   | e1           | e2   | e3   | e1             | e2   | e3   |
| Sol-U<br>(TOA) | Mean   | 14.6            | 34.2 | 31.2 | -3.4         | 15.9 | 8.5  | 16.6           | 29.1 | 22.3 |
|                | Median | 11.6            | 27.4 | 23.7 | 0.0          | 10.8 | 5.7  | 13.1           | 22.8 | 17.6 |
|                | RMSE   | 29.6            | 45.7 | 44.0 | 20.8         | 32.8 | 28.8 | 26.0           | 39.2 | 32.0 |
|                | SD     | 25.8            | 30.3 | 31.1 | 20.4         | 28.6 | 27.5 | 20.0           | 26.2 | 23.0 |
| Sol-D<br>(SFC) | Mean   | -11.6           | 0.8  | 3.1  | 17.6         | 21.7 | 20.0 | -20.8          | -8.4 | 0.6  |
|                | Median | -6.3            | 1.6  | 3.3  | 2.6          | 4.9  | 6.5  | -8.3           | -2.3 | -1.1 |
|                | RMSE   | 57.4            | 55.3 | 51.9 | 52.8         | 56.4 | 49.4 | 54.6           | 47.5 | 28.7 |
|                | SD     | 56.3            | 55.3 | 51.8 | 49.8         | 52.1 | 45.2 | 50.5           | 46.7 | 28.7 |